Quadrupole collectivity in the neutron-rich sulfur isotopes math xmlns="http://www.w3.org/1998/Math/MathML">mmultiscripts>mi mathvariant="normal">S/mi> mprescripts>/mprescripts>none>/none>mrow>mn>38/mn>mo>,/mo>mn>40/mn>mo>,/mo>mn>42/mn>mo>,/mo>mn>44/mn>/mrow>/mmultiscripts>/math>

B. Longfellow, D. Weisshaar, A. Gade, B. A. Brown, D. Bazin, K. W. Brown, B. Elman, J. Pereira, D. Rhodes, and M. Spieker

Phys. Rev. C **103**, 054309 — Published 18 May 2021

DOI: 10.1103/PhysRevC.103.054309

Quadrupole collectivity in the neutron-rich sulfur isotopes ^{38,40,42,44}S

B. Longfellow,[1,2,3] D. Weisshaar,[1] A. Gade,[1,2] B. A. Brown,[1,2] D. Bazin,[1,2]
K. W. Brown,[1,4] B. Elman,[1,2] J. Pereira,[1] D. Rhodes,[1,2] and M. Spieker[1,*]

[1] *National Superconducting Cyclotron Laboratory, Michigan State University, East Lansing, Michigan 48824, USA*
[2] *Department of Physics and Astronomy, Michigan State University, East Lansing, Michigan 48824, USA*
[3] *Lawrence Livermore National Laboratory, Livermore, California 94550, USA*
[4] *Department of Chemistry, Michigan State University, East Lansing, Michigan 48824, USA*

(Dated: April 22, 2021)

Electromagnetic transition strengths in the even-even neutron-rich sulfur isotopes ^{38,40,42,44}S were measured using intermediate-energy Coulomb excitation at the National Superconducting Cyclotron Laboratory. By utilizing the sensitivity of the experimental technique to $E2$ excitations from the ground state, the evolution of the pattern of $B(E2)$ strengths to several low-lying 2^+ states was investigated at $Z = 16$ from near stability to the $N = 28$ island of inversion. The experimental results allowed a detailed comparison with predictions from shell-model calculations using the SDPF-MU Hamiltonian, which was designed to describe collectivity in this region of the nuclear chart. While the shell-model calculations succeeded in modeling transition strengths at $N = 22, 24, 26$, the experimental $B(E2; 0_1^+ \rightarrow 2_1^+)$ at $N = 28$ was smaller than the predicted value by about a factor of two, similar to previous observations for chlorine and argon isotopes around $N = 28$. The dependence of this overprediction by theory on the choice of effective charges was explored.

I. INTRODUCTION

The neutron-rich sulfur isotopes approaching the conventional neutron magic number $N = 28$ have attracted a considerable amount of experimental and theoretical attention that has provided great insight into how nuclear shell structure is modified far from the valley of stability [1, 2]. Due to the narrowing of the $N = 28$ gap via shell evolution, particle-hole intruder configurations become lower in energy and compete with the normal-order configurations leading to the phenomena of shape and configuration coexistence [3]. In fact, at the center of the so-called $N = 28$ island of inversion [4], ^{42}Si [5, 6] and ^{44}S [7] show characteristics of deformation and collective behavior indicative of an absent shell closure.

The first evidence for the breakdown of the $N = 28$ magic number was provided by the observation of moderate $B(E2; 0_1^+ \rightarrow 2_1^+)$ strengths in ^{40,42}S [8] and ^{44}S [7] through intermediate-energy Coulomb excitation. Further studies of ^{44}S have suggested the coexistence of a prolate-deformed ground state and a spherical 0_2^+ excited state at 1365 keV [9, 10]. In addition, lifetime measurements in ^{44}S [11, 12] and supporting theoretical calculations [13, 14] have established the coexistence of levels dominated by zero-, one-, and two-neutron particle-hole configurations at low excitation energy.

In a recent in-beam γ-ray spectroscopy measurement, an interesting systematic trend for the $2_2^+ \rightarrow 0_1^+$ and $2_2^+ \rightarrow 2_1^+$ γ-ray branching ratios in the sulfur isotopic chain was observed by Lunderberg *et al.* and discussed in comparison with shell-model calculations [15]. Shell-model calculations using the SDPF-MU interaction [16] predict that for ^{38}S and ^{40}S, the $2_2^+ \rightarrow 2_1^+$ transitions will dominate with 96.4% and 99.4% branching ratios, respectively. In ^{42}S, the reverse occurs with a prediction of 84.2% for the $2_2^+ \rightarrow 0_1^+$ transition and only 15.8% for the $2_2^+ \rightarrow 2_1^+$ transition. These shell-model predictions were validated experimentally with the non-observation of the $2_2^+ \rightarrow 0_1^+$ branch in ^{38}S [15, 17] and a measurement of 85(2)% for the tentative $(2_2^+) \rightarrow 0_1^+$ branch in ^{42}S [15]. The shell-model calculations link the abrupt change in decay pattern for ^{42}S with the difference in occupancies for the neutron $0f_{7/2}$ and $1p_{3/2}$ orbitals for the 2_1^+ and 2_2^+ states. In addition, a dramatic increase in level density for 0^+ and 2^+ states below 4.5 MeV in ^{44}S (see Figure 20 of [15]) signals the sudden and massive gain in correlation energy of the intruder configuration formed by moving two neutrons into the $1p_{3/2}$ orbital compared to the closed $0f_{7/2}$ shell configuration, placing ^{44}S inside of the $N = 28$ island of inversion with ^{42}S right at the boundary. Due to this particular interplay of the single-particle configurations, a measurement of the $B(E2)$ excitation strengths to higher-lying 2^+ states provides a unique window into the breakdown of the $N = 28$ shell gap at $Z = 16$ and the underlying driving forces that are a cornerstone in explaining shell evolution in rare isotopes.

In this work, intermediate-energy Coulomb excitation was used to populate both first and higher-lying 2^+ states in the even-even sulfur isotopes from $N = 22$ to 28. At intermediate energies, predominantly quadrupole collective states are excited in a single step from the initial level [18, 19], making this technique optimal for selectively populating 2^+ levels connected to the ground state by $E2$ transitions. $B(E2)$ strengths from the ground state to the 2_1^+ states for ^{38,40,42}S [8] and ^{44}S [7] were first measured using intermediate-energy Coulomb excitation over 20 years at the National Superconducting Cyclotron Laboratory using an array of NaI(Tl) detectors and a plastic

* Present address: Department of Physics, Florida State University, Tallahassee, Florida 32306, USA.

phoswich detector. Here, we present the second measurements of the $B(E2;0_1^+ \rightarrow 2_1^+)$ strength for ^{38,40,44}S using any experimental technique. Furthermore, the increase in secondary beam rates available since the experiments described in [7, 8] were performed made the first measurements of $B(E2)$ strengths from the ground state to 2^+ levels beyond the lowest-energy 2^+ states in these nuclei possible. Consequently, the observed feeding of the 2_1^+ levels from higher-lying 2^+ states could be accounted for in the analysis for the first time.

The measured $B(E2)$ strengths were used to test in detail the predictions of shell-model calculations using the SDPF-MU effective interaction [16], which was developed in the years since the previous sulfur Coulomb excitation measurements [7, 8]. The SDPF-MU Hamiltonian was constructed to describe the shell and shape evolution in the sulfur and silicon isotopic chains toward $N = 28$, in order to provide an important step toward confirming the underlying mechanism of shell evolution suggested by the most successful effective Hamiltonian in this region. In recent works, the reported one-proton knockout cross sections to ^{42}Si states [20] and proton inelastic scattering cross sections measured for ^{41,43}P [21] were best reproduced in shell-model calculations using SDPF-MU. In $N = 27$ ^{43}S, the predicted $B(E2)$ strengths from shell-model calculations using the SDPF-MU interaction and the SDPF-U interaction [22], which was also developed to describe the $N = 28$ island of inversion, were similar [23]. Furthermore, theoretical calculations exploring the role of effective charges were performed to address the overprediction of theoretical $B(E2)$ strengths near $N = 28$. This long-standing issue was observed here for ^{44}S and previously for ^{43}S [23], ^{45}Cl [24], ^{46}Ar [8, 25, 26], and ^{47}Ar [27].

II. EXPERIMENT

The intermediate-energy Coulomb excitation experiment was performed using the Coupled Cyclotron Facility at the National Superconducting Cyclotron Laboratory [28]. First, a primary beam of stable ^{48}Ca accelerated to 140 MeV/u. The ^{38,40,42,44}S secondary beams were produced in separate allotments of beam time by fragmentation of the primary beam on a ^{9}Be production target at the midacceptance position of the A1900 fragment separator [29]. All secondary beams were purified using a 450 mg/cm^2 achromatic Al wedge degrader. For each set of runs, the sulfur secondary beam of interest was then impinged on a 492 mg/cm^2 ^{209}Bi target at the reaction target position of the S800 magnetic spectrograph [30] to inelastically excite the sulfur nuclei via the Coulomb interaction. At mid-target, the energies for ^{38,40,42,44}S were 75, 76, 80, and 73 MeV/u, respectively. Slits in the beamline were used to restrict the momentum acceptance to about 1% for ^{38,40,42}S and 2% for ^{44}S.

Plastic timing scintillators and the standard set of S800 focal-plane detectors [31] were used to identify the outgoing reaction products and to reconstruct their trajectories on an event-by-event basis. The scattering angles of the projectiles at the reaction target were reconstructed using information from the two xy-position sensitive cathode-readout drift chambers (CRDCs) in the S800 focal plane and knowledge of the S800 magnetic rigidity. An example of the particle identification plot using energy loss in the S800 ionization chamber and the time of flight between plastic scintillators in the beamline and at the back of the S800 focal plane for the ^{44}S setting is shown in Figure 1. The vertical line spanning energy loss at a constant time of flight above the ^{44}S gate is due to pileup in the ionization chamber. The total number of pileup counts at the time of flight corresponding to ^{44}S is less than 3% of the counts in the energy loss peak. The vertical line below the ^{44}S gate at a constant time of flight is about an order of magnitude suppressed relative to the number of pileup counts. These counts can be attributed to ^{44}S nuclei undergoing reactions on one of the four CRDC foils or the ionization chamber entrance foil, which add up to a total of about 20 mg/cm^2 of poly p-phenylene terephthalamide ($C_{14}H_{14}N_2O_4$).

The lower-Z reaction products lose less energy in the ionization chamber but the time of flight is retained since the CRDCs and ionization chamber entrance are close to the end of the flight path. For ^{38,40,42}S, the secondary beam intensities were restricted by the rate limit at the S800 focal plane. For ^{44}S, the average secondary beam intensity was about 3900 pps.

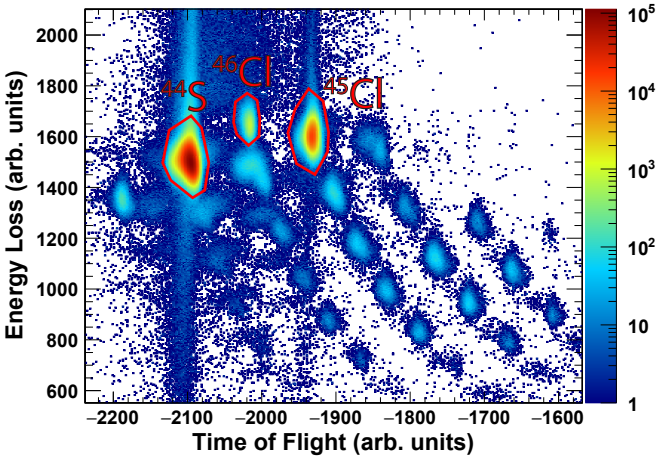

FIG. 1. Particle identification plot utilizing energy loss and time of flight for the ^{44}S setting. The energy loss is measured in the S800 ionization chamber and is proportional to Z^2 and the time of flight measured between plastic scintillators in the beam line and at the back of the S800 focal plane and is proportional to A/Z.

At intermediate beam energies, the analysis of Coulomb excitation experiments must be restricted to a maximum scattering angle or equivalently a minimum impact parameter. This minimum impact parameter is typically chosen to exceed the sum of the radii of the pro-

jectile and target nuclei by several fm so that the electromagnetic contribution to the inelastic excitation cross section dominates [25, 32–34]. Due to the high velocity of the projectile, the time spent in the vicinity of the target nucleus is short, greatly suppressing multistep excitations [18]. Therefore, for even-even nuclei, 2^+ states with a sufficiently $E2$ connection with the ground state are selectively populated in single-step excitations. The scattering angles of the sulfur projectiles were measured using the CRDCs

The experimental cross sections for populating the 2^+ states via Coulomb excitation were determined by detecting the in-flight γ-ray de-excitations from the sulfur projectiles. To do this, the ^{209}Bi reaction target was surrounded by the CAESium-iodide scintillator ARray CAESAR [35], a 192-element array of CsI(Na) detectors covering nearly 4π and providing high efficiency and granularity. The cross sections were used to extract the electric quadrupole transition strength $B(E2)$ assuming the Coulomb excitation mechanism. In particular, the relativistic model of Coulomb excitation developed by Alder and Winther [18] was utilized. The reduced transition strengths obtained from intermediate-energy Coulomb excitation experiments using this method, including experiments at similar beam energies and in the same mass region as the present results, have shown excellent agreement with the results found using other experimental probes [33].

To model the in-beam response of CAESAR after Doppler reconstruction, GEANT4 simulations benchmarked against laboratory-frame spectra from standard γ-ray calibration sources were utilized. The simulated efficiency curve was scaled to match the measured efficiency curve following the method of [36], introducing a 5% systematic uncertainty [37]. The intrinsic and in-beam energy resolutions of CAESAR as a function of γ-ray energy are discussed in Ref. [35]. To determine Coulomb excitation cross sections from the de-excitation γ-ray yields, no addback procedure was applied to the singles spectra for CAESAR in order to avoid additional systematic uncertainties on the γ-ray detection efficiency. However, the gain in statistics afforded by nearest-neighbor addback was exploited in the γ-γ plots used to identify coincidences and in the multiplicity-one plots used to identify ground-state transitions.

III. RESULTS

For each of the nuclei ^{38,40,42,44}S, the Doppler-corrected γ-ray spectra were fit with GEANT4 simulations of the lineshapes of observed γ-ray transitions and GEANT4 simulations of Doppler-corrected 511-keV and 1460-keV laboratory-frame background lines together with a double exponential background. These fits were performed using several choices for the maximum scattering angle. Note that the GEANT4 simulations take into account the small changes in detection efficiency with choice of scattering angle cut due to the anisotropic angular distribution of the emitted γ rays. The angle-integrated cross sections, determined from the efficiency-corrected γ-ray yields, number of incoming S projectiles, and reaction target thickness, were then converted to $B(E2)$ strengths using the Alder-Winther model of relativistic Coulomb excitation. In each case, a more restrictive maximum scattering angle cut than the nominal maximum safe scattering angle as determined from the touching spheres plus 2 fm prescription for the minimum safe impact parameter was utilized due to the angular spread of the beam and angular straggling in the target [36, 38].

For $2^+_x \rightarrow 2^+_1$ decays, there are contributions from both $M1$ and $E2$ multipoles. Since the multipole mixing ratio affects the angular distribution of the emitted γ rays, there is an effect on the detection efficiency of the array. The quoted $B(E2)$ strengths were extracted using the predicted multipole mixing ratios from shell-model calculations using the SDPF-MU interaction. From GEANT4 simulations of CAESAR for the 1513-keV $2^+_2 \rightarrow 2^+_1$ transition in ^{38}S, the difference in efficiency using the angular distribution predicted from the shell-model multipole mixing ratio compared to assuming a pure $E2$ transition is about 0.1%. The SDPF-MU multipole mixing ratios were used to determine the angular distributions for all mixed transitions in this work. In addition, proton and neutron effective charges of 1.35 and 0.35, respectively, [16] were utilized for these SDPF-MU shell-model calculations.

The uncertainties for transition energies were derived from the fit uncertainties added in quadrature with a systematic uncertainty of 4.5 keV [39]. For the $2^+_1 \rightarrow 0^+_1$ transitions, the reported energies are from fits to the non-addback spectra with more restrictive choices of scattering angle. For the $2^+_x \rightarrow 2^+_1$ transitions, the reported energies are from fits to the projections of the $\gamma-\gamma$ coincidence matrices with nearest-neighbor addback employed and no scattering angle cut applied. The uncertainty in energy for the $2^+_2 \rightarrow 0^+_1$ transition in ^{42}S was found by fitting the multiplicity-one nearest-neighbor addback spectrum.

A. ^{38}S

The Doppler-corrected γ-ray spectrum for ^{38}S measured with CAESAR is provided in Figure 2 with a laboratory-frame scattering angle cut of 40 mrad applied. The low-energy region of the spectrum is dominated by bremsstrahlung, which is electromagnetic radiation produced by the acceleration of electrons from the target atoms due to interactions with the beam, and other beam-correlated background such as target breakup and reaction products interacting with the beampipe. The highest intensity peak corresponds to the known $2^+_1 \rightarrow 0^+_1$ transition in ^{38}S at 1292.0(2) keV [40]. The energy of the transition measured in this work is 1289(5) keV.

The weak γ-ray peaks at 1513 keV and 2508 keV were included on the basis of γ-γ coincidence data.

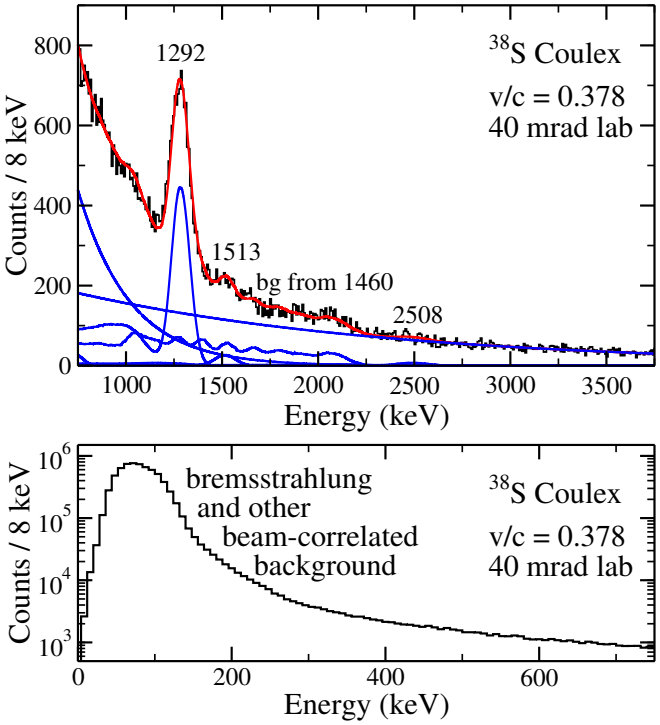

FIG. 2. Top: Doppler-corrected energy spectrum for ^{38}S gated on scattering angles smaller than 40 mrad in the laboratory frame. The blue curves are the individual components of the fit function derived from GEANT4 simulations along with a double exponential background. The 1292-keV $2_1^+ \rightarrow 0_1^+$ transition, 1513-keV $2_2^+ \rightarrow 2_1^+$ transition, and 2508-keV $2_3^+ \rightarrow 2_1^+$ transition were included in the fit. The red curve is the total fit function. Bottom: Low-energy portion of the Doppler-corrected energy spectrum for ^{38}S. The large background at low energies is due to bremsstrahlung and other beam-correlated background.

The background-subtracted projection of the γ-γ coincidence matrix gated on the 1292-keV peak is shown in Figure 3. As seen in the figure, the 1292-keV transition is in coincidence with transitions at 1513 keV and 2508 keV. The background subtraction was performed by gating on a projection of the same width as the 1292-keV gate but at higher energy and subtracting the resulting spectrum from the 1292-keV projection. The 1513-keV peak has been observed previously and tentatively assigned as the $(2_2^+) \rightarrow 2_1^+$ transition [15, 17, 41–43]. The adopted energy for the transition is 1513(2) keV [40] and the energy measured here is 1512(9) keV. Its observation from intermediate-energy Coulomb excitation in this work confirms the 2_2^+ assignment. The 2508(25)-keV transition from a level at 3800(25) keV has not been observed in previous works. Shell-model calculations using the SDPF-MU interaction predict that the 2_3^+ level in ^{38}S is at 3553 keV in excitation energy and decays with a relative branching ratios of 100% to the 2_1^+, 18% to the ground state and 18% to the 2_2^+ level. This is consistent with the 2508-1292 keV cascade from a 3800-keV level established here. Due to low statistics, any additional γ-decay branches from the 3800-keV state were not observed.

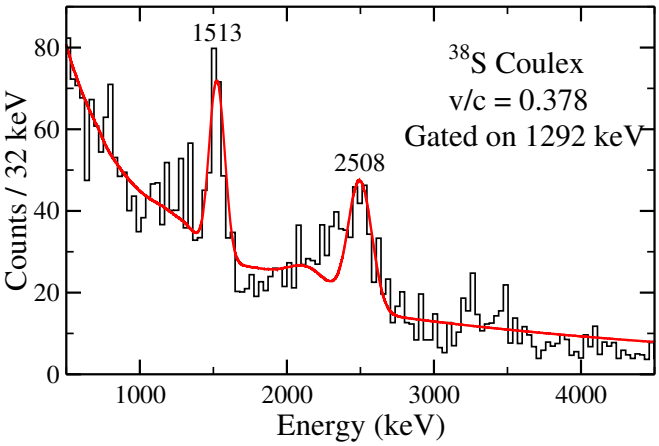

FIG. 3. Background-subtracted, Doppler-corrected γ-ray spectrum for ^{38}S counts in coincidence with the 1292-keV $2_1^+ \rightarrow 0_1^+$ transition. The 1513-keV and 2508-keV transitions are visible and included in the red fit curve derived from GEANT4 simulations.

The nominal maximum safe scattering angle is 55 mrad in the laboratory frame, as determined from the touching spheres plus 2 fm prescription for the minimum safe impact parameter. While the uncertainty in the angle measurement due to the position resolution of the CRDCs is about 2 mrad [31], the angular spread of the incoming beam is on the order of 5-10 mrad. Figure 4 shows the number of background-subtracted counts in the 1292-keV full-energy peak as a function of scattering angle in the laboratory frame. At the nominal safe scattering angle cut of 55 mrad, the experimental data fall below the Alder-Winther prediction, which does not account for the angular spread in the incoming beam or angular straggling in the target, prompting a more restrictive choice for the maximum of 40 mrad. The angle-integrated cross section for the 1292-keV transition as a function of scattering angle cut is shown in the top panel of Figure 5. Note that the top panel of Figure 5 is essentially proportional to the angular integration of the counts in Figure 4. In practice, the cross sections in the top panel of Figure 5 were determined from the efficiency-corrected γ-ray yields of fits similar to that shown in Figure 2. Here, the cross sections have been corrected for the feeding contributions of the 1513-keV and 2508-keV transitions. The corresponding $B(E2; 0_1^+ \rightarrow 2_1^+)$ strengths calculated using the semiclassical approach of Alder and Winther are shown in the bottom panel of Figure 5. Up until about 40 mrad, the extracted $B(E2; 0_1^+ \rightarrow 2_1^+)$ values are rather constant, while for larger scattering cuts they start to decrease, reflecting the deviation from the Alder-Winther

prediction seen in Figure 4.

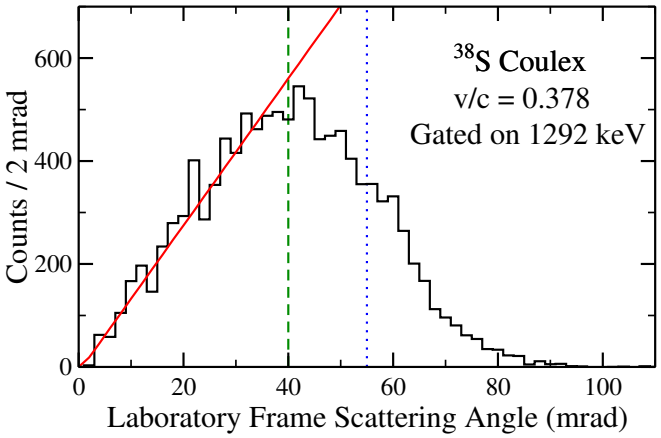

FIG. 4. Counts in the 1292-keV peak as a function of scattering angle in the laboratory frame. The red curve is from the Alder-Winther model and does not include the effects of the angular spread in the beam or angular straggling in the target. Consequently, a maximum scattering angle of 40 mrad was considered in the analysis rather than the nominal safe scattering angle of 55 mrad.

Using a maximum scattering angle of 40 mrad in the laboratory frame, the $B(E2;0_1^+ \rightarrow 2_1^+)$ strength was determined to be 229(19) e^2fm^4. Similarly, the $B(E2;0_1^+ \rightarrow 2_2^+)$ strength was found to be 21(8) e^2fm^4 and the $B(E2;0_1^+ \rightarrow 2_3^+)$ strength was found to be 11(8) e^2fm^4 for the same maximum scattering angle.

The value for the $B(E2;0_1^+ \rightarrow 2_1^+)$ strength from the previous intermediate-energy Coulomb excitation experiment by Scheit *et al.* is 235(30) e^2fm^4 [8]. The 1513-keV and 2508-keV feeding transitions were not observed by Scheit *et al.* due to limited statistics. If feeding is neglected in this analysis, the extracted $B(E2;0_1^+ \rightarrow 2_1^+)$ strength is 261 e^2fm^4, which is also consistent with the previous value [8].

B. ^{40}S

The known $2_1^+ \rightarrow 0_1^+$ transition in ^{40}S at 903.68(9) keV [40] is clearly visible in the Doppler-corrected γ-ray energy spectrum with a laboratory-frame scattering angle cut of 40 mrad applied shown in Figure 6. The energy of the transition measured in this work is 902(5) keV. In addition, there is a weak transition at 2452(23) keV. The 2452-keV transition is more clearly observed in the background-subtracted projection of the two-dimensional γ-γ coincidence matrix gated on 904 keV shown in Figure 7. From this coincidence relationship, the 2452(23)-keV transition is inferred to originate from a level at 3356(23) keV.

The angle-integrated cross section for the 904-keV transition, corrected for feeding by the 2452-keV transition, is shown in the top panel Figure 8 as a function

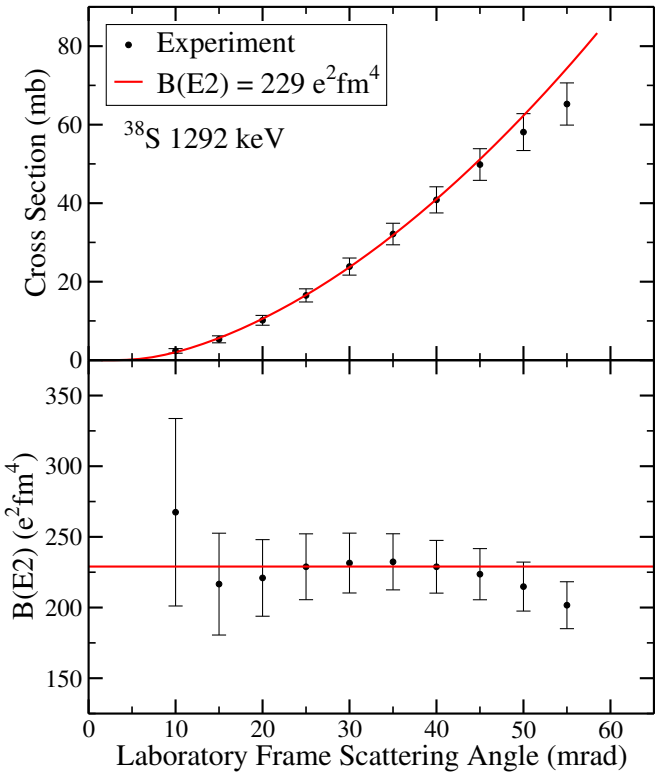

FIG. 5. Top: feeding-subtracted, angle-integrated cross section as a function of choice of scattering angle cut derived from the experimental data for the 2_1^+ state in ^{38}S (black circles). The red curve is the expected cross section assuming a $B(E2;0_1^+ \rightarrow 2_1^+)$ strength of 229 e^2fm^4. Bottom: $B(E2;0_1^+ \rightarrow 2_1^+)$ strength calculated using the Alder-Winther model of Coulomb excitation for different choices of maximum scattering angle.

of scattering angle cut. The nominal maximum scattering angle in the laboratory frame is 51 mrad. The bottom panel shows the corresponding $B(E2;0_1^+ \rightarrow 2_1^+)$ values. The $B(E2;0_1^+ \rightarrow 2_1^+)$ strength adopted in this work is 284(26) e^2fm^4 using the more conservative 30 mrad laboratory-frame scattering angle cut. The value for the $B(E2;0_1^+ \rightarrow 2_1^+)$ strength reported by Scheit *et al.* from an intermediate-energy Coulomb excitation experiment, in which no feeding was observed due to limited statistics, is 334(36) e^2fm^4 [8]. If feeding from the 2452-keV transition is neglected in this work, the extracted $B(E2;0_1^+ \rightarrow 2_1^+)$ strength is 305 e^2fm^4, which is consistent with the previous measurement within uncertainties.

SDPF-MU shell-model calculations for ^{40}S predict that the 2_2^+ level is at 3285 keV and that the 2_3^+ state is at 3579 keV. The 2_2^+ state in the calculation decays nearly 100% of the time to the 2_1^+ level. Similarly, the 2_3^+ state decays with a relative 100% branch to the 2_1^+ level and an 8% branch to the ground state. However, the predicted $B(E2;0_1^+ \rightarrow 2_2^+)$ strength is only 2.9 e^2fm^4 compared to 54 e^2fm^4 for the $B(E2;0_1^+ \rightarrow 2_3^+)$ strength. The experimental $B(E2;0_1^+ \rightarrow 2_x^+)$ strength for the 3356(23)-keV

state calculated from the yield of the 2452-keV transition in this work is 26(17) e^2fm^4 using the 30 mrad scattering angle cut. No higher-lying 2^+ states beyond the first 2^+ are listed in the current data evaluation [40].

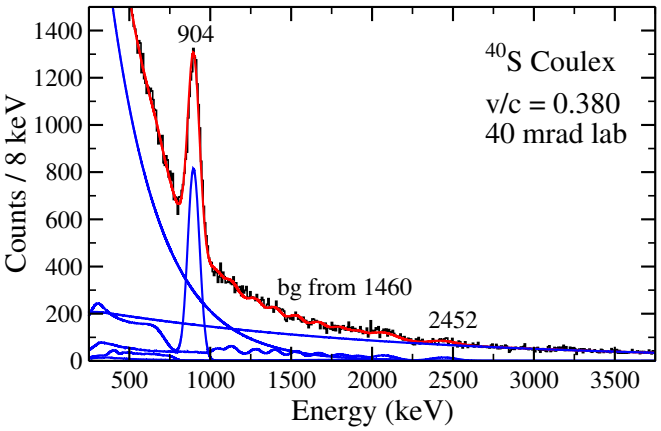

FIG. 6. Doppler-corrected energies of ^{40}S γ rays measured with CAESAR. A scattering angle cut of 40 mrad in the laboratory frame has been applied. The red curve is the total fit function and the blue curves are the individual components of the fit function derived from GEANT4 simulations along with a double exponential background. The 904-keV $2_1^+ \rightarrow 0_1^+$ transition and 2452-keV $2_x^+ \rightarrow 2_1^+$ transition were included in the fit.

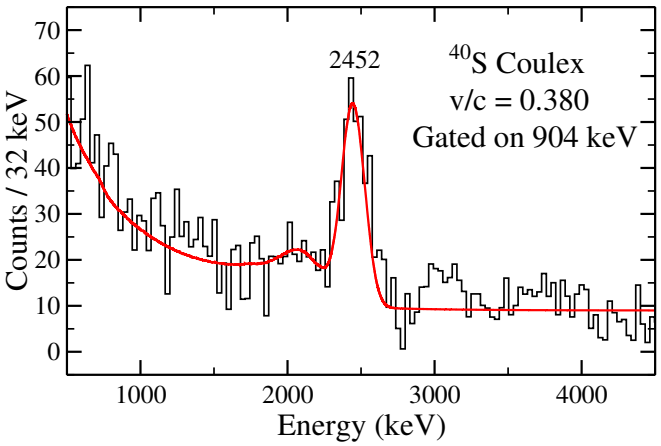

FIG. 7. Background-subtracted, Doppler-corrected γ-ray spectrum for ^{40}S gated on coincidences with the 904-keV transition from the 2_1^+ level to the ground state. The red fit curve from GEANT4 simulations includes the clearly-seen 2452-keV transition.

C. ^{42}S

The 2_1^+ state in ^{42}S has been reported at 903(5) keV [40]. In this work, γ rays corresponding to the $2_1^+ \rightarrow 0_1^+$ transition are clearly seen in Figure 9, the non-addback Doppler-corrected γ-ray spectrum measured with CAESAR using a scattering angle cut of 40 mrad in the laboratory frame. The energy of the transition extracted from the fit performed in this experiment is 904(5) keV, in good agreement with the literature value.

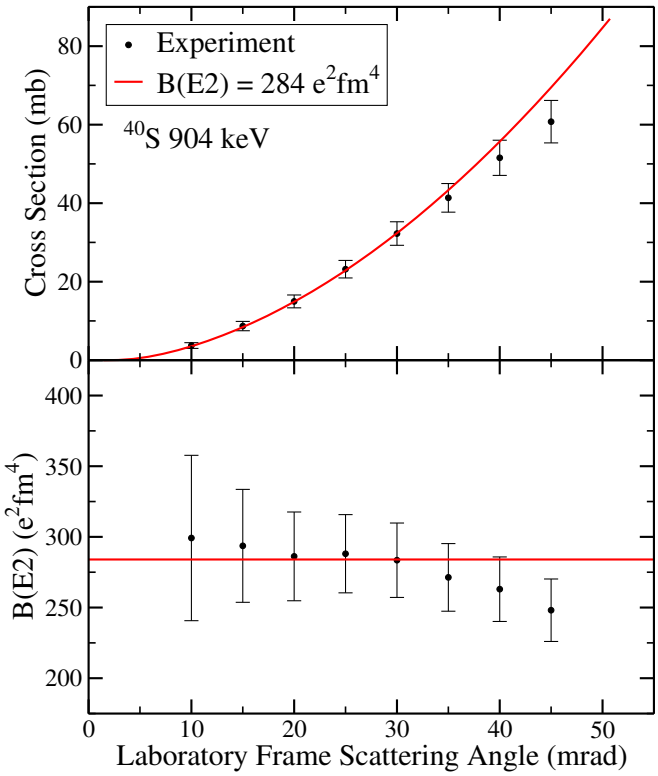

FIG. 8. Top: angle-integrated cross section as a function of scattering-angle cut for the feeding-subtracted experimental data on the 2_1^+ state in ^{40}S (black circles). The expected cross section assuming a $B(E2; 0_1^+ \rightarrow 2_1^+)$ strength of 284 e^2fm^4 is represented by the red curve. Bottom: $B(E2; 0_1^+ \rightarrow 2_1^+)$ strength calculated using Alder and Winther's model of Coulomb excitation for different choices of maximum scattering angle.

Lunderberg *et al.* observed a 3002(4) keV γ ray in ^{42}S and tentatively associated this transition with the decay from the (2_2^+) state to the ground state [15]. This transition can be seen at 3005(13) keV in the nearest-neighbor addback spectrum gated on multiplicity one events shown in Figure 10. For an array like CAESAR covering nearly the full solid angle, the relative enhancement of the 3002-keV peak for events where only one γ ray was detected (a so-called multiplicity one event) compared to all events is indicative of a direct transition to ground state. The observation of the 3002-keV transition in intermediate-energy Coulomb excitation in this work confirms the assignment by Lunderberg *et al.* rather than the proposal for the (2_2^+) level lying at 2779 keV and decaying predominantly to the 2_1^+ state put forth by Sohler *et al.* [44].

From [15], the 3002-keV level has relative decay

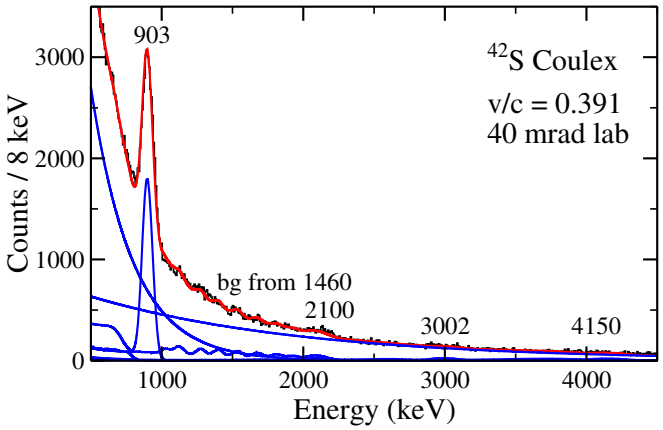

FIG. 9. ^{42}S Doppler-corrected energy spectrum measured by CAESAR for scattering angles smaller than 40 mrad in the laboratory frame. The blue curves are the individual components of the fit function derived from GEANT4 simulations along with a double exponential background while the red curve is the total fit function. The 903-keV $2_1^+ \rightarrow 0_1^+$ transition, 2100-keV $2_2^+ \rightarrow 2_1^+$ transition, 3002-keV $2_2^+ \rightarrow 0_1^+$ transition, and 4150-keV $2_x^+ \rightarrow 2_1^+$ transition (see discussion in text) were included in the fit.

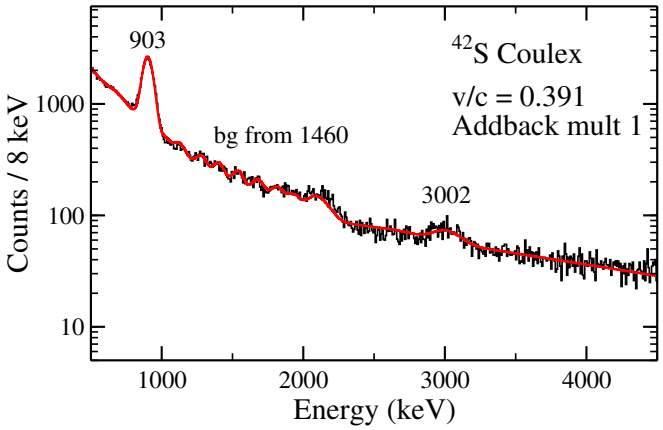

FIG. 10. Doppler-corrected energy spectrum for ^{42}S for events where only one γ ray was detected by CAESAR. Nearest-neighbor addback was utilized. The 3002-keV transition from the 2_2^+ state to the ground state is visible and included in the red fit curve derived from GEANT4 simulations.

branches of 100(2)% to the ground state and 18(2)% to the 2_1^+ state via a 2100(4)-keV γ-ray transition. As seen in Figure 11, the 2100-keV peak is visible in the background-subtracted projection of the two-dimensional γ-γ coincidence matrix gated on the 903-keV transition along with a broad feature around 4150(110) keV. The energy of the 2100-keV transition measured in this work is 2117(31) keV, consistent with the more precise value of 2100(4) keV from [15]. Due to the broad feature originating from Doppler-corrected 1460-keV background, the relative intensities of the 3002-keV and 2100-keV transitions were fixed to the known efficiency-corrected branching ratio from [15] in the fit of Figure 9 and in the similar fits performed using different scattering angle cuts.

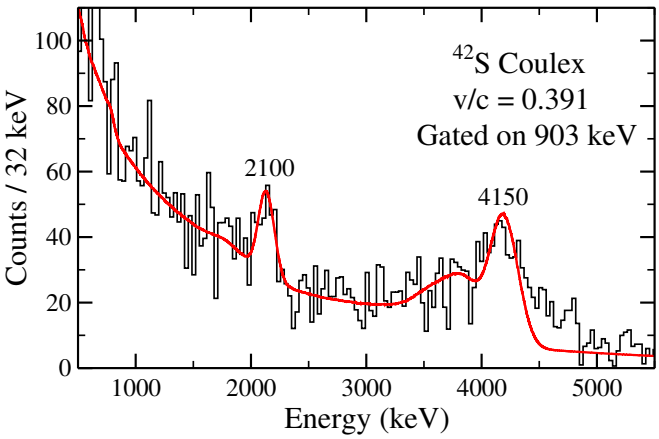

FIG. 11. Coincidences with the 903-keV $2_1^+ \rightarrow 0_1^+$ transition in ^{42}S. This spectrum has been background subtracted and Doppler corrected. A peak at 2100 keV and a feature around 4150 keV are visible and included in the red fit curve derived from GEANT4 simulations. See text for discussion.

Figure 12 shows the angle-integrated cross section for the 903-keV transition as a function of scattering angle cut. The cross sections have been corrected for feeding from the 2100-keV and 4150-keV transitions. Unlike for ^{38}S and ^{40}S, this plot shows a clear and significant dependence of extracted $B(E2; 0_1^+ \rightarrow 2_1^+)$ strength on laboratory-frame scattering angle cut for all choices of maximum scattering angle. A method similar in principle to the CRDC scaling method introduced in [45, 46] was developed to remove this dependence. In [45, 46], the low statistics of a nucleus of interest and low CRDC efficiency prevented the direct application of a maximum scattering angle cut. Instead, the intermediate-energy Coulomb excitation cross section for a high-statistics contaminant in the same setting as a function of maximum scattering angle was utilized. The ratios of cross sections at different maximum scattering angles to the total cross section with no scattering angle cut for the high-statistics contaminant were determined. Then, the same ratios were applied to the cross section for the nucleus of interest with no scattering angle cut to estimate the cross sections and $B(E2)$ values at the given maximum scattering angle cuts. Therefore, in this method, the shapes of the cross section curves as a function of maximum scattering angle for the contaminant and nucleus of interest were assumed to be the same within experimental uncertainties.

Here, a high-statistics contaminant in the ^{42}S setting was not available so we instead use the shape of the theoretical cross section curve as a function of maximum scattering angle, which is fixed by the A and Z of the target and projectile, multipolarity of the transition, energy of the state being excited, and velocity of the beam at mid-target. The experimental cross section curve should have

the same shape over the range of scattering angles smaller than the scattering angle at which the angular straggling begins to affect the data, as seen in Figure 5 for ^{38}S and Figure 8 for ^{40}S. The $B(E2;0_1^+ \rightarrow 2_1^+)$ strength is proportional to the scaling factor of the curve. The theoretical cross section was parameterized as $a_t\theta^2 + b_t\theta + c_t$ where θ is the maximum scattering angle. Similarly, the experimental data were parameterized as $a_e\theta^2 + b_e\theta + c_e$ for experimental laboratory-frame scattering angles from 10 mrad to 35 mrad. A quadratic modification factor was then applied to the experimental scattering angles where the value of this factor was chosen to minimize $(a_t/b_t - a_e/b_e)^2$. Since the minimization is based on the ratios a_t/b_t and a_e/b_e, the shape of the experimental curve is adjusted to match the shape of the theoretical curve without matching the absolute scaling. Therefore, the $B(E2;0_1^+ \rightarrow 2_1^+)$ strength is not assumed beforehand in the modification procedure. The best fit scaling factor for the theoretical curve after modifying the experimental data corresponds to a $B(E2;0_1^+ \rightarrow 2_1^+)$ strength of 326 e^2fm^4.

The ^{42}S data were taken in two separate sets of beam time, one in the middle of the experiment and one at the end of the experiment. The data from the first set and the second set show the same correlation between $B(E2;0_1^+ \rightarrow 2_2^+)$ strength and laboratory scattering angle shown in Figure 12. For example, the cross sections found for the 40 mrad laboratory-frame scattering angle cut from the first and second data sets are 48.4 mb and 48.2 mb, respectively. The experimental data for each of the neutron-rich sulfur isotopes was taken in the following order: ^{38}S, ^{40}S, ^{42}S (first half), ^{43}S (see [23, 37]), ^{44}S, and ^{42}S (second half). The ^{43}S data [23, 37] and ^{44}S data discussed later do not clearly show the same correlation between choice of scattering angle cut and $B(E2;0_1^+ \rightarrow 2_2^+)$ strength observed for ^{42}S. Therefore, the issue did not appear at a certain time and persist for the remainder of the experiment. Based on this, it is hypothesized that the problem is with the scattering-angle reconstruction on an incoming beam basis rather than a scattering-angle-dependent loss in γ-ray detection efficiency.

The $B(E2;0_1^+ \rightarrow 2_1^+)$ in ^{42}S measured in intermediate-energy Coulomb excitation by Scheit *et al.* was 397(63) e^2fm^4 [8]. The lifetime of the 2_1^+ state in ^{42}S has also been measured using the recoil-distance method to be 20.6(15) ps [12] and $21.5^{+1.1}_{-0.9}$ ps [47]. Using an excitation energy of 903(5) keV, the corresponding $B(E2;0_1^+ \rightarrow 2_1^+)$ strengths are 329(26) e^2fm^4 from [12] and 315^{+18}_{-16} e^2fm^4 from [47]. The value of 326 e^2fm^4 found after applying the modification to the scattering angle is in very good agreement with these previous measurements. The uncertainty in the extracted $B(E2;0_1^+ \rightarrow 2_1^+)$ strength was estimated by varying the number of experimental data points included in the fit and using both linear and quadratic modification factors. Including an additional 10% systematic uncertainty, the adopted value is 326(48) e^2fm^4. Since this value is close to the uncertainty-weighted average from the previous measurements of 323 e^2fm^4, the $B(E2)$ values to the higher-lying 2^+ states reported below are the same as those calculated relative to the previously-measured $B(E2;0_1^+ \rightarrow 2_1^+)$ strength.

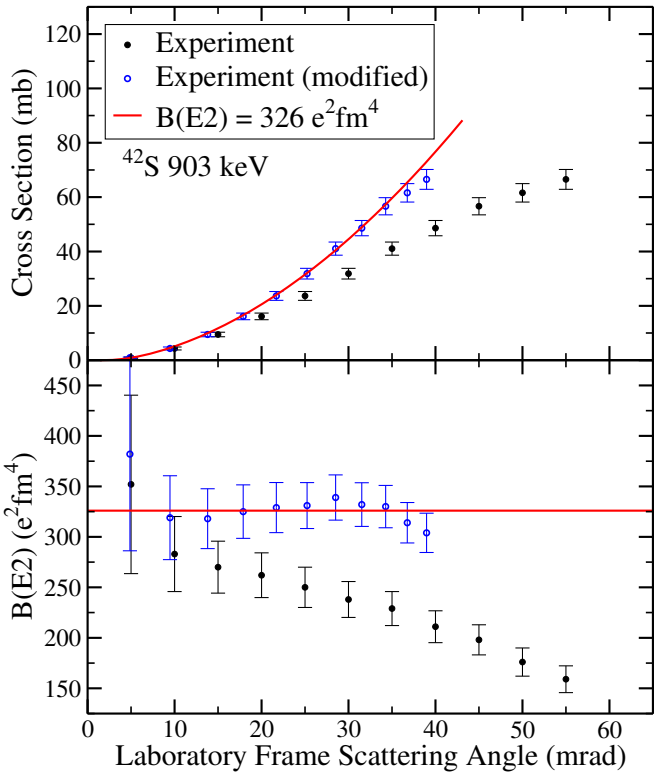

FIG. 12. Top: experimental feeding-subtracted and angle-integrated cross section as a function of scattering-angle cut for the 2_1^+ state in ^{42}S (black circles). The red curve is the predicted cross section for a $B(E2;0_1^+ \rightarrow 2_1^+)$ strength of 326 e^2fm^4. The blue data points are the experimental data with the modification for scattering angle explained in the text. Bottom: $B(E2;0_1^+ \rightarrow 2_1^+)$ strength for different choices of maximum scattering angle calculated using the Alder-Winther model of Coulomb excitation.

The Coulomb excitation cross section to the 3002-keV state was found using the 35 mrad laboratory-frame scattering angle cut from the yields of the detected 2100-keV and 3002-keV de-excitation γ rays. The $B(E2;0_1^+ \rightarrow 2_2^+)$ strength was calculated using the same modified scattering angle used to extract the adopted result for the $B(E2;0_1^+ \rightarrow 2_1^+)$ strength to be 27(14) e^2fm^4. SDPF-MU shell-model calculations predict a $B(E2;0_1^+ \rightarrow 2_5^+)$ strength of 16 e^2fm^4 for the level at 5003 keV. The predicted reduced transition strengths to the 2_3^+ and 2_4^+ states are less than 0.001 e^2fm^4 and about 4 e^2fm^4, respectively. The 2_4^+ level at 4924 keV decays with a relative branching ratios of 100% to the ground state and 54% branching ratio to the 2_1^+ state (with smaller branching ratios to other states) while the 2_5^+ level decays with relative branching ratios of 100% to the 2_1^+ state and

11% to the ground state in the calculation. Employing the same method used for the 3002-keV level, the reduced transition strength to the level at 5053(110) keV that decays via a 4150(110)-keV γ ray to the 903-keV 2_1^+ state was calculated to be 11(9) e^2fm^4 assuming an $E2$ excitation from the data using the 35 mrad scattering angle cut. Lunderberg *et al.* report γ-ray transitions at 4102(8) keV and 4266(7) keV that were not placed in the level scheme [15]. Due to its large energy uncertainty, the 4150(110)-keV feature may correspond to one or a combination of these transitions.

D. ^{44}S

Figure 13 shows the Doppler-corrected spectrum of γ rays measured with CAESAR in coincidence with ^{44}S projectiles at the S800 focal plane. Here, a laboratory-frame scattering angle cut of 40 mrad was employed. The previously-observed 1329.0(5)-keV γ ray corresponds to the $2_1^+ \rightarrow 0_1^+$ transition [10]. Other works report the energy of this transition as 1297(18) keV [7], 1350(10) keV [44], 1319(7) keV [11], 1321(10) keV [48], and 1320(8) keV [49]. The energy of the transition measured in this work is 1324(6) keV. The 949(5)-keV $2_3^+ \rightarrow 2_1^+$ transition reported in the literature [40] is more clearly observed in the background-subtracted projection of the two-dimensional γ-γ coincidence matrix gated on 1329 keV for events with exactly two detected γ rays shown in Figure 14. The energy for the $2_3^+ \rightarrow 2_1^+$ transition measured in this work is 941(19) keV. This transition has also been reported recently at an energy of 954(4) keV [21]. SDPF-MU shell-model calculations predict that the 2_3^+ state decays with relative branching ratios of 100% to the 2_1^+ level and 14% to the ground state. Due to low statistics, the possible ground state branch was not observed in this experiment or in previous works. The 2150(11)-keV transition reported in the literature is tentatively assigned as the γ decay of the 2_2^+ state to the ground state [11, 12]. Due to the Doppler-corrected 1460-keV laboratory-frame background, the possible presence of this transition in this work is not well constrained.

The angle-integrated cross section for the 1329-keV transition, corrected for feeding by the 949-keV transition, is shown in the top panel Figure 15 as a function of the choice of maximum scattering angle. As seen in the bottom panel of Figure 15, the corresponding $B(E2; 0_1^+ \rightarrow 2_1^+)$ strength does not decrease with scattering angle cut with the same large slope observed for ^{42}S. Furthermore, ^{45}Cl nuclei were present as a component of the cocktail incoming secondary beam in the ^{44}S setting. The $B(E2)$ strength measured in this experiment from the $(1/2^+)$ ground state of ^{45}Cl to the $(5/2^+)$ level at 928(9) keV was 82(29) e^2fm^4 using a laboratory-frame scattering angle cut of 40 mrad [37]. This result is in excellent agreement with the previous intermediate-energy Coulomb excitation measurement of 87(24) e^2fm^4 [24] providing additional evidence that the

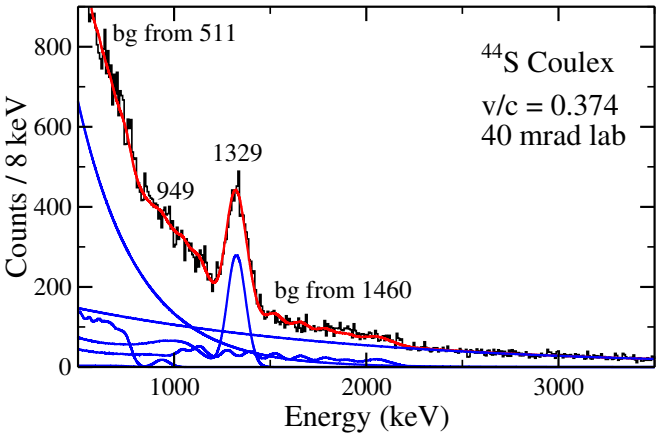

FIG. 13. Doppler-corrected energy spectrum for the ^{44}S projectiles identified in the S800 gated on scattering angles smaller than 40 mrad in the laboratory frame. The red curve shows the total fit function. The blue curves are the individual components of the fit function derived from GEANT4 simulations along with a double exponential background. The 1329-keV $2_1^+ \rightarrow 0_1^+$ transition and 949-keV $2_3^+ \rightarrow 2_1^+$ transition were included in the fit.

modification necessary for ^{42}S is not required for ^{44}S. The $B(E2; 0_1^+ \rightarrow 2_1^+)$ strength extracted for ^{44}S using a 35 mrad laboratory-frame scattering angle cut is 221(28) e^2fm^4. The nominal maximum scattering angle in the laboratory frame from the touching spheres plus 2 fm approximation is 48 mrad. Using the same angle cut and the yield of the 949-keV $2_3^+ \rightarrow 2_1^+$ transition, the $B(E2; 0_1^+ \rightarrow 2_3^+)$ strength was determined to be 10(6) e^2fm^4.

The $B(E2; 0_1^+ \rightarrow 2_1^+)$ strength reported from intermediate-energy Coulomb excitation by Glasmacher *et al.* is 314(88) e^2fm^4 [7] which overlaps with the value in this work of 221(28) e^2fm^4 within mutual uncertainties. No feeding transitions were observed in the work of Glasmacher *et al.* [7]. If feeding is neglected in this work, the $B(E2; 0_1^+ \rightarrow 2_1^+)$ value increases to 231 e^2fm^4, slightly improving the agreement.

IV. DISCUSSION

A. $B(E2)$ strengths in the even neutron-rich sulfur isotopes

In general, the $B(E2; 0_1^+ \rightarrow 2_1^+)$ strengths extracted in this work for ^{38,40,42,44}S are slightly lower than those published by Scheit *et al.* [8] and Glasmacher *et al.* [7], as seen in Table I. In the previous works, transitions feeding the 2_1^+ states were not observed due to limited statistics preventing feeding subtraction from being performed when determining the excitation cross sections. Furthermore, the $B(E2; 0_1^+ \rightarrow 2_1^+)$ strengths in ^{42}S calculated from recent lifetime measurements of 329(26) e^2fm^4

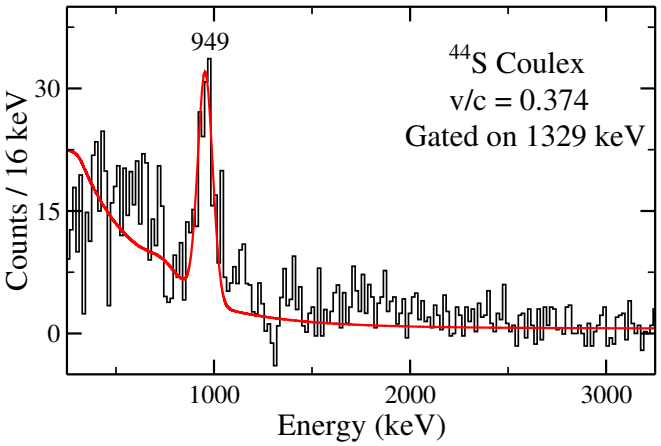

FIG. 14. Doppler-corrected γ-ray spectrum in coincidence with the 1329-keV transition from the 2_1^+ level to the ground state in ^{44}S. Background subtraction has been applied. The 949-keV transition can be seen and is included in the red fit curve derived from GEANT4 simulations.

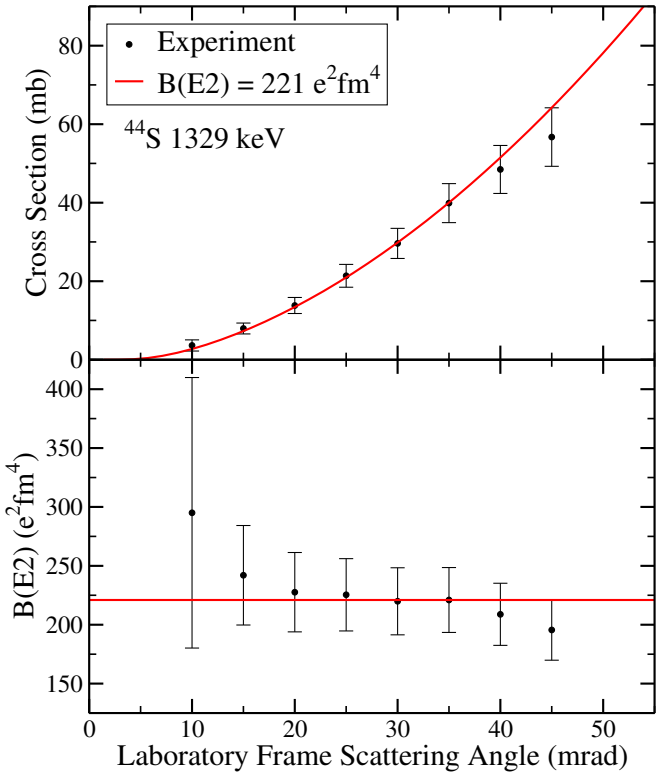

FIG. 15. Top: measured feeding-subtracted, angle-integrated cross section for the 2_1^+ state in ^{44}S as a function of choice of maximum scattering angle cut (black circles). The theoretical cross section for a $B(E2;0_1^+ \rightarrow 2_1^+)$ strength of 221 e^2fm^4 is shown in red. Bottom: $B(E2;0_1^+ \rightarrow 2_1^+)$ strength calculated for different choices of maximum scattering angle using the model of Coulomb excitation developed by Alder and Winther.

[12] and 315^{+18}_{-16} e^2fm^4[47] are slightly below the value of 397(63) e^2fm^4 from Scheit *et al.* and are in good agreement with the value of 326(48) e^2fm^4 found in the present work. Figure 16 shows a visual comparison of the measured $B(E2)$ strengths and the $B(E2)$ strengths predicted using shell-model calculations with the SDPF-MU interaction for several 2^+ states. Overall, there is very good agreement in both the pattern and magnitude of the excitation strengths between experiment and theory from $N = 22$ to $N = 26$. However, at $N = 28$, the experimental value for the $B(E2;0_1^+ \rightarrow 2_1^+)$ strength is about a factor of two lower than the predicted value.

TABLE I. $B(E2)$ strengths for the neutron-rich sulfur isotopes studied in this work compared to the results of previous intermediate-energy Coulomb excitation experiments and theoretical calculations using the SDPF-MU Hamiltonian with effective proton and neutron charges of 1.35 and 0.35, respectively.

^{A}S	Excitation	This Work e^2fm^4	Prior Work e^2fm^4	SDPF-MU e^2fm^4
^{38}S	$0_1^+ \rightarrow 2_1^+$	229(19)	235(30) [8]	160
	$0_1^+ \rightarrow 2_2^+$	21(8)		25
	$0_1^+ \rightarrow 2_3^+$	11(8)		26
^{40}S	$0_1^+ \rightarrow 2_1^+$	284(26)	334(36) [8]	300
	$0_1^+ \rightarrow 2_2^+$			3
	$0_1^+ \rightarrow 2_3^+$	26(17)		54
^{42}S	$0_1^+ \rightarrow 2_1^+$	326(48)	397(63) [8]	370
	$0_1^+ \rightarrow 2_2^+$	27(14)		38
	$0_1^+ \rightarrow 2_5^+$	11(9)		16
^{44}S	$0_1^+ \rightarrow 2_1^+$	221(28)	314(88) [7]	450
	$0_1^+ \rightarrow 2_2^+$			12
	$0_1^+ \rightarrow 2_3^+$	10(6)		11

In ^{38}S, the $B(E2;0_1^+ \rightarrow 2_2^+)$ strength was measured as 21(8) e^2fm^4 from the 1513-keV $2_2^+ \rightarrow 2_1^+$ transition while the reduced transition strength from the ground state to the newly-observed level at 3800(25) keV was found to be 11(8) e^2fm^4 from the 2508-keV transition to the 2_1^+ state. Based on comparison to the theoretical calculations (see Figure 16 and Table I), the newly-observed 3800(25)-keV level is inferred to have structure most similar to the shell-model 2_3^+ state. The 2_2^+ state at 2805 keV was observed to γ decay to the 2_1^+ level but not to the ground state, consistent with the previous experimental measurements [15, 17] and with the dominance of the $2_2^+ \rightarrow 2_1^+$ branch predicted by SDPF-MU shell-model calculations.

For ^{40}S, the reduced transition probability from the ground state to the presumed 2^+ level at 3356(23) keV was found to be 26(17) e^2fm^4. Based on its observation in this work, the 3356(23)-keV level corresponds more closely to the collective shell-model 2_3^+ state shown in Figure 16 and Table I. The predicted relative branching ratios for the 2_3^+ state are 100% to the 2_1^+ level and 8% to the ground state. Here, only the $2_3^+ \rightarrow 2_1^+$ branch of the newly-reported 3356(23)-keV state was observed,

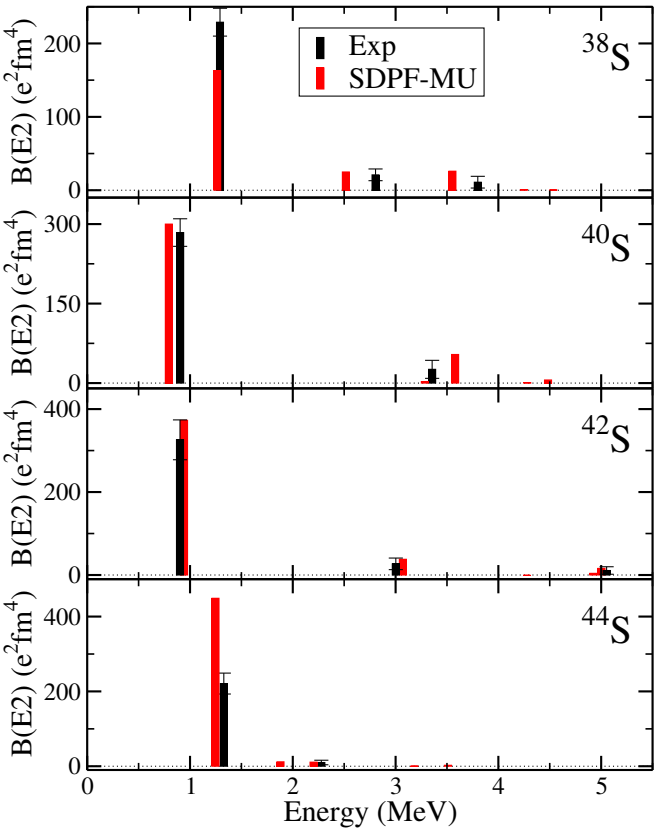

FIG. 16. $B(E2;0_1^+ \rightarrow 2^+)$ strengths in the even-even sulfur isotopes for the 2^+ states measured in this work compared to predictions from shell-model calculations utilizing the SDPF-MU Hamiltonian for the first five 2^+ states.

consistent with the theoretical predictions given the level of statistics. The 2_2^+ state is predicted to decay to the 2_1^+ level with a 99.4% branching ratio but has a predicted $B(E2;0_1^+ \rightarrow 2_2^+)$ value of only 2.9 e^2fm^4 compared to the predicted $B(E2;0_1^+ \rightarrow 2_3^+)$ value of 54 e^2fm^4. In the single-particle picture discussed by Lunderberg *et al.* [15], the neutron $1p_{3/2}$ occupancy for the ground state is very similar to the neutron $1p_{3/2}$ occupancies for the 2_1^+ and 2_3^+ states, both of which states were observed in the present work. The SDPF-MU neutron $1p_{3/2}$ occupancy of the unobserved 2_2^+ level is only slightly higher but is nearly identical to the neutron $1p_{3/2}$ occupancy of the 0_2^+ state, which is predicted to be at nearly the same excitation energy (see Figure 20 of Ref. [15]).

As seen in Table I for ^{42}S, SDPF-MU shell-model calculations predict a $B(E2;0_1^+ \rightarrow 2_2^+)$ strength of 38 e^2fm^4 compared to the measured value of 27(14) e^2fm^4. The branching ratios of the tentatively assigned 2_2^+ level at 3002-keV to the 2_1^+ state and the ground state measured by Lunderberg *et al.* were in remarkable agreement with the predictions from SDPF-MU shell-model calculations [15]. Here, the 3002-keV state was confirmed as the 2_2^+ level. Therefore, both the rapid change in decay pattern for the 2_2^+ state from ^{40}S to ^{42}S and the quadrupole collectivity of the 2_2^+ state are successfully captured in shell-model calculations using the SDPF-MU interaction. The shell-model calculations also predict a $B(E2;0_1^+ \rightarrow 2_5^+)$ strength of 16 e^2fm^4. Assuming an $E2$ excitation, the reduced transition strength to the level observed in the present work at 5053(110) keV is 11(9) e^2fm^4. However, the 4150(110)-keV transition from the 5053(110)-keV state may correspond to multiple unresolved transitions, such as the 4102-keV and 4266-keV transitions reported in [15]. Overall, the predictions from shell-model calculations using the SDPF-MU Hamiltonian for the energies of 2^+ states and $B(E2)$ strengths in ^{42}S are in very good agreement with the experimental results, as seen in Figure 16, supporting the single-particle evolution sketched with the neutron $1p_{3/2}$ occupancy in Figure 20 of [15].

For $N = 28$ ^{44}S, the $B(E2;0_1^+ \rightarrow 2_2^+)$ and $B(E2;0_1^+ \rightarrow 2_3^+)$ strengths from the shell-model calculation are 12 e^2fm^4 and 11 e^2fm^4, respectively (see Table I). The experimental value for the $B(E2;0_1^+ \rightarrow 2_3^+)$ strength measured from the 949-keV transition of the 2278-keV state is 10(6) e^2fm^4 while the yield of possible 2150-keV transitions from the decay of the 2_2^+ level to the ground state was not well constrained due to Doppler-corrected 1460-keV laboratory-frame background.

From the experimental results in the present work, the $B(E2;0_1^+ \rightarrow 2_1^+)$ strength peaks at $N = 26$ for the sulfur isotopes between $N = 22$ and $N = 28$. Shell-model predictions using SDPF-MU, however, put the maximum collectivity at $N = 28$ rather than $N = 26$ over this range of neutron numbers. The SDPF-MU $B(E2;0_1^+ \rightarrow 2_1^+)$ strengths for ^{44}S and ^{46}S are nearly the same at about 450 e^2fm^4 while the SDPF-MU $B(E2;0_1^+ \rightarrow 2_1^+)$ strength for ^{48}S is lower at around 330 e^2fm^4. The measured $B(E2;0_1^+ \rightarrow 2_1^+)$ strength of 221(28) e^2fm^4 for ^{44}S is roughly half of the predicted value.

Overall, the experimental $B(E2)$ strengths and branching ratios measured in this work indicate that the picture of shape and configuration coexistence in the transition into the $N = 28$ island of inversion painted by shell-model calculations using the SDPF-MU Hamiltonian is largely supported. Detailed tests for the predictions of shapes will be possible through low-energy Coulomb excitation experiments with FRIB beam rates. In addition, experimental evidence has mounted showing that single-particle strengths in this region seem to be well-described by shell-model calculations using SDPF-MU and SDPF-U, which were both developed to describe the $N = 28$ island of inversion, suggesting that the evolution of the single-particle shell gaps is properly captured (see e.g. [10, 20, 48–52]). Therefore, the observed disagreement in $B(E2;0_1^+ \rightarrow 2_1^+)$ strength at $N = 28$ may be related to the effective charges utilized in the shell-model calculations as discussed in the following subsection.

B. Collectivity around $N = 28$ within the shell model

Shell-model calculations also overpredict $B(E2)$ strengths in sulfur at $N = 27$. In ^{43}S, the $B(E2; 3/2^-_1 \rightarrow 7/2^-_2)$ strength of 91(18) e^2fm^4 [23, 37], measured in the same experiment as the results reported here, is two times smaller than the value of 181 e^2fm^4 from calculations with the SDPF-MU Hamiltonian (using proton and neutron effective charges of 1.35 and 0.35, respectively) and about three times smaller than the value of 284 e^2fm^4 predicted from shell-model calculations using the SDPF-U effective interaction (using proton and neutron effective charges of 1.5 and 0.5, respectively) [22]. The $B(E2; 7/2^-_1 \rightarrow 9/2^-_1)$ strength for ^{43}S is 101(42) e^2fm^4 [23, 37], which is smaller than but still consistent within uncertainty with the SDPF-MU prediction of 137 e^2fm^4. The prediction from shell-model calculations using SDPF-U for the $B(E2; 7/2^-_1 \rightarrow 9/2^-_1)$ strength is 191 e^2fm^4. The same phenomenon has been observed at $Z = 17$ as well. Shell-model calculations using SDPF-MU predict $B(E2)$ strengths from the $1/2^+$ ground state to the $3/2^+_2$ and $5/2^+_1$ states in $N = 28$ ^{45}Cl of 159 and 153 e^2fm^4, respectively. However, the $1/2^+_1$ and $3/2^+_1$ states in ^{45}Cl are within 200 keV in the calculation and the spin-parities of the ground and first-excited states have not been clearly established experimentally [48, 53, 54]. The theoretical $B(E2)$ strengths from the $3/2^+_1$ state to the $3/2^+_2$ and $5/2^+_1$ states are 83 and 148 e^2fm^4. In the intermediate-energy Coulomb excitation experiments reported here and in [24], only the $(5/2^+_1)$ state was excited from the ground state with measured $B(E2)$ strengths of 82(29) and 87(24)e^2fm^4, respectively, which are both around a factor of two smaller than both the $1/2^+_1 \rightarrow 5/2^+_1$ and $3/2^+_1 \rightarrow 5/2^+_1$ shell-model predictions. The $(3/2^+_2)$ level was not clearly observed in either experiment.

Furthermore, a similar overprediction of the $B(E2; 0^+_1 \rightarrow 2^+_1)$ strength by shell-model calculations has been reported for $N = 28$ ^{46}Ar, two protons above ^{44}S. While a lifetime measurement obtained a value of 570^{+335}_{-160} e^2fm^4 [55], intermediate-energy Coulomb excitation experiments have resulted in consistent strengths of 196(39) e^2fm^4 [8], 218(31) e^2fm^4 [25], and 225(29) e^2fm^4 (absolute) and 234(19) e^2fm^4 (relative to ^{44}Ca) [26]. Shell-model calculations with several interactions including SDPF-MU predict a $B(E2; 0^+_1 \rightarrow 2^+_1)$ strength roughly a factor of two larger at over 500 e^2fm^4 [26]. Likewise, the $B(E2)$ strength from the $3/2^-$ ground state to low-lying states for $N = 29$ ^{47}Ar [27] are overpredicted by shell-model calculations using the SDPF-U and EPQQM interactions [56] by roughly a factor of two. At $N = 30$, the reported $B(E2; 0^+_1 \rightarrow 2^+_1)$ strength of 346(55) e^2fm^4 is in better agreement with theoretical calculations but is still about 1.5 to 2 standard deviations lower than predicted [27].

The proton and neutron effective charges were varied in order to examine their effect on the calculated $B(E2)$ strengths using different shell-model interactions. The model space consisting of $(0d_{5/2}, 0d_{3/2}, 1s_{1/2})(sd)$ for protons and $(0f_{7/2}, 0f_{5/2}, 1p_{3/2}, 1p_{1/2})(fp)$ for neutrons was utilized. The SDPF-MU [16] and SDPF-U Hamiltonians [22] were developed in this model space for nuclei in the mass region we consider. Both of these Hamiltonians give good agreement with experiment for energy spectra and one-nucleon transfer properties for the nuclei we consider (see Ref. [57], for example). For the $E2$ matrix elements we use harmonic-oscillator radial wavefunctions with $\hbar\omega = 45A^{-1/3} - 25A^{-2/3}$.

The limitation of the valence shell model is most obviously manifest in the electric quadrupole ($E2$) observables. The valance orbitals contribute only part of the $E2$ matrix elements. The $E2$ matrix elements for the valence space must be supplemented by effective charges. The bare value of the charge e for a proton and 0 for a neutron are modified to $e_p = (1 + \delta_p)e$ for a proton and $e_n = (0 + \delta_n)e$ for a neutron. The δ are usually treated as parameters to best reproduce the $B(E2)$ data for a given model space. The empirical values for δ for three model spaces are given in Table II. These are the sd model space with $8 \leq Z, N \leq 20$ for protons and neutrons [58], the fp model space with $20 \leq Z, N \leq 60$ for protons and neutrons [59], and the $sd - pf$ model space with $(8 \leq Z \leq 20)$ and protons $20 \leq N \leq 60$ for neutrons [16]. It is observed that the δ parameters are model space dependent.

In Figure 17, we compare the experimental $B(E2; 0^+_1 \rightarrow 2^+_1)$ values for Ca, Ar, and S isotopes with different choices for the effective charges. The first is obtained by taking the proton effective charge from the sd shell (δ_p=0.37) and the neutron effective charge from the fp shell (δ_n=0.50). The second is obtained using the empirical values of $\delta_p = \delta_n = 0.35$ for the $sd - pf$ model space [16]. As expected, the data are in best agreement with the results obtained with the smaller proton effective charge that was adjusted for this set of nuclei.

TABLE II. Empirical proton and neutron effective charges (e_p and e_n) used by shell-model interactions in different model spaces.

Model Space	Mass Region	e_p	e_n	Ref
sd (pn)	^{28}Si	1.37	0.45	[58]
fp (pn)	^{56}Ni	1.5	0.5	[59]
sd (n), fp (p)	^{40}S	1.35	0.35	[16]

We investigate the origin of the model-space dependence of δ by using a microscopic model that is based on theoretical work done in the 1970's [61]. We evaluate the core-polarization diagrams shown in Figure 18. In the original models, the vertical lines represent the valence orbital. Diagram (A) represents the interaction of the valence proton with the $E2$ operator (the x). Diagrams (B) and (C) are the first-order core-polarization corrections, representing the admixture of proton particle-hole

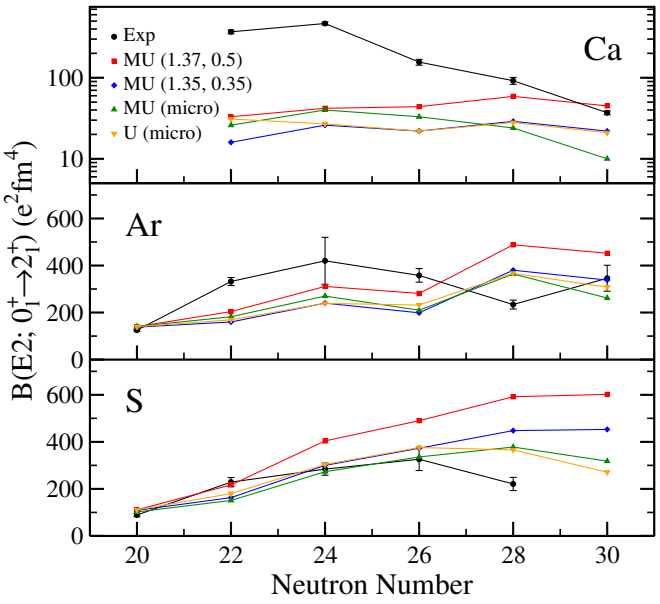

FIG. 17. $B(E2;0_1^+ \rightarrow 2_1^+)$ predictions for the Ca, Ar, and S isotopic chains from shell-model calculations using the SDPF-MU Hamiltonian using different values for the proton and neutron effective charges compared to experimental results. SDPF-MU (1.37, 0.5) (red) uses $e_p = 1.37$ (effective sd shell value from Table II) and $e_n = 0.5$ (effective fp shell value from Table II). SDPF-MU (1.35, 0.35) (blue) uses $e_p = 1.35$ and $e_n = 0.35$ as recommended in Ref. [16]. SDPF-MU (micro) (green) uses the microscopic effective charges of Table III calibrated to reproduce $e_p = 1.37$ at $N = 20$ and $e_n = 1.50$ at ^{56}Ni. SDPF-U (micro) (orange) is the same as SDPF-MU (micro) except the SDPF-U Hamiltonian is used. The $B(E2)$ strengths for ^{46}Ar and ^{48}Ar are from Ref. [26] and Ref. [27], respectively. Experimental values for ^{38,40,42,44}S are taken from this work. All other experimental values come from Ref. [60].

states into the initial (B) and final states (C). For δ_p the vertical line is a valence proton, and for δ_n the vertical line is a valence neutron. The horizontal line is the interaction that connects the valence nucleon with the proton particle-hole states. The selection rules for $E2$ in the harmonic-oscillator limit the contribution of particle-hole configurations to those that are $2\hbar\omega$ higher in energy. These are same configurations that contribute to the giant quadrupole excitation.

We calculate δ with the model used in [61] that was obtained with a delta-function interaction. In [61] these diagrams were calculated for single-particle or single-hole valence states where there is a sharp Fermi surface surface between the proton particles and holes. The results for some closed-shell configurations are given in Table III. The polarization charges depend on the closed shell for protons and on the $(n,\ell)-(n',\ell')$ of the valance orbitals. In particular the average neutron effective charges for ^{42}Si is smaller than those for ^{56}Ni. The neutron valence transition density associated with the vertical lines in Figure 18 is the same, but the transition density associated with the proton particles and holes peaks at a smaller radius for ^{42}Si compared to ^{56}Ni. This qualitatively explains the Z dependence of the phenomenological neutron effective charge parameters in Table II.

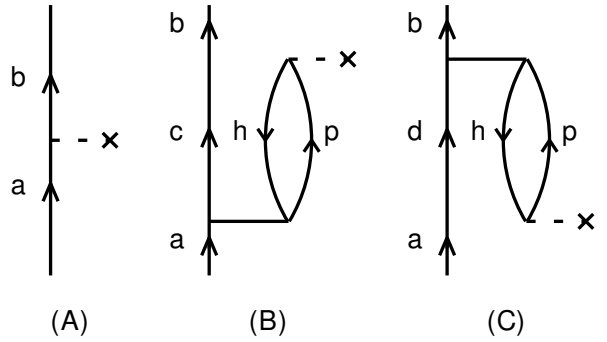

FIG. 18. Diagrammatic representation of core-polarization for a valence proton. The vertical lines represent the initial (a) and final (b) valence orbital with intermediate states (c) and (d). Diagram (A) represents the interaction of the valence proton with the $E2$ operator (the x). Diagrams (B) and (C) are the first-order core-polarization corrections, representing the admixture of proton particle-hole (p-h) states into the initial (B) and final (C) states, respectively.

In this work we generalize the model of [61] by replacing the vertical lines in Figure 18 with the complete of set of valence one-body transition densities together with a Fermi surface that depends on the proton orbital occupancies in each nucleus. This increases the number of proton orbitals that contribute to the transition by about a factor of five. The δ become nucleus and state dependent. The results compared to the experimental data are shown in Figure 17. It is observed that the microscopic results are similar to those obtained with the smaller effective charge of δ_p=0.35. As seen in Table III, the δ_p values for $1p-0f$ are smaller because of the node in their valence transition density [61]. This was idea was used to explain the relatively small $B(E2)$ observed for the $1/2^+$ to $5/2^+$ transition in ^{21}O that is dominated by the valence $1s-0d$ valence neutron transition density [62].

TABLE III. Microscopic neutron effective charges (e_n) calculated from $0f-0f$, $0f-1p$, and $1p-1p$ neutron-neutron two-body interactions for different nuclei.

Two-body Interaction	^{56}Ni	$^{40-48}$Ca [61]	^{42}Si
$0f-0f$	0.56	0.45	0.30
$0f-1p$	0.49	0.32	0.21
$1p-1p$	0.38	0.28	0.13

The valance transition densities for $N = 28$ have relatively large contributions from $1p_{3/2} - 0f_{7/2}$ neutrons.

However, other valence orbitals also contribute. The small microscopic effective charge for $1p-0f$ is not enough to explain why the experimental $B(E2)$ drop at $N=28$ compared to the increase in theory.

A striking aspect of the comparison between experiment and theory is observed for the Ca isotopes. For $^{42-44}$Ca the observed $B(E2)$ are an order of magnitude large than the calculations in the fp model space for neutrons. It is well known that this is due to mixing with low-lying "intruder" states that come from the excitations of protons from the sd shell to the fp shell. For example, for ^{42}Ca the dominant configuration is $4p-2h$ with two proton holes in the sd shell and an alpha-cluster type $4p$ configuration in the pf shell. The proton part of the $B(E2)$ from this intruder admixture completely overwhelms the small fp shell neutron contribution. Models have been developed that include these sd to pf admixtures [63, 64]. These models are in better agreement with experiment but are still differ by up to factors of 2-3 [65]. However, the practical applications of these models is at present restricted to nuclei near ^{40}Ca.

In contrast, the experimental $B(E2)$ values for ^{48,50}Ca are by far the smallest in this mass region and they are only about a factor of two larger than the fp model space calculations. This change from ^{42}Ca to ^{48}Ca is related to the diminished mixing of sd with pf proton excitations. In ^{42}Ca the excitation energy of the $4p-2h$ proton configuration is almost degenerate with that of the $2p$ (neutron) configuration. In ^{48}Ca the 2^+ state at 3.81 MeV is associated with the $8p$ valence neutron configuration for the $B(E2)$ given in Figure 17. The energy of the $10p-2h$ proton excitation may be associated with the 0^+ state at 4.28 MeV and the 2^+ state at 5.31 MeV [66]. We are not aware of microscopic calculations that describe the $B(E2)$ values in ^{48}Ca associated with $10p-2h$ states and their mixing with the $8p$ configuration.

A pattern similar to the calcium isotopes has been observed for the oxygen isotopes. The $B(E2)$ values for ^{18,20}O are strongly enhanced by mixing with configurations coming from the excitation of protons form the p shell to the sd shell. This mixing becomes smaller as the number of neutrons increases. As discussed above, the $B(E2)$ observed for ^{21}O [62] is consistent with that expected from the microscopic calculations that result in a relatively small neutron effective charge for the $1s-0d$ component of the $E2$ matrix elements. The equivalent transition for the calcium isotopes is the $3/2^-$ to $7/2^-$ transition in ^{49}Ca, where only a lower limit on the lifetime of the $3/2^-$ state is known. This should be measured.

Taking into account these observations for the Ca isotopes, we can interpret the comparison between experiment and theory for the argon and sulfur isotopes. The ^{40,42,44}Ar experimental $B(E2)$ strengths are about 50% larger than those calculated. This is probably associated with the mixing of sd to fp proton excitations in parallel to ^{42,44,46}Ca. The increase is not as dramatic as the factor of ten observed for Ca because the valence space already contains some proton contribution and perhaps because the mixing with sd to fp proton configurations is smaller.

Our purpose for carrying out the relatively simple core-polarization calculations was to investigate the qualitative aspects of core-polarization. From this we were able to understand the model-space dependence of the average effective proton effective charge. As discussed above, there is an orbital dependence to the effective charge, but this is not enough to explain the deviation between experiment and theory at $N=28$ for Ar and S. The microscopic theory can be improved by using more realistic interactions, including higher-order diagrams, and using more realistic radial wavefunctions. These improvements should be investigated with regard to understanding the difference between experiment and theory at $N=28$. For instance, VS-IMSRG models similar to those used recently for the Si isotopes out to $N=28$ [67] should be used for the S and Ar isotopes.

V. SUMMARY

The technique of intermediate-energy Coulomb excitation was used to probe electric quadrupole transition strengths from the ground states to the first 2^+ excited states and to higher-lying 2^+ levels in the neutron-rich sulfur isotopes ^{38,40,42,44}S. In general, the excitation energies and $B(E2)$ values predicted from shell-model calculations using the SDPF-MU effective interaction were in good agreement with the experimental results for ^{38,40,42}S. For $N=28$ ^{44}S, however, the theoretical calculations overpredict the $B(E2;0_1^+\rightarrow 2_1^+)$ strength by about a factor of two. This fits into a picture of similar overpredictions by theory around $N=28$ in the nearby chlorine and argon isotopes. We discuss a possible explanation for this observation in terms of the model space dependence of the effective charges that are needed in shell-model frameworks. The distribution of experimental $B(E2)$ strengths in the rapidly changing sulfur isotopic chain will serve as important benchmarks for any nuclear model that aims to describe the development of collectivity in the $N=28$ island of inversion.

ACKNOWLEDGMENTS

This work was supported by the National Science Foundation (NSF) under Grants No. PHY-1102511 and PHY-1565546, by the DOE National Nuclear Security Administration through the Nuclear Science and Security Consortium, under Award No. DE-NA0003180, and by the Department of Energy, Office of Nuclear Physics, under Grant No. DE-SC0020451. Work at LLNL was performed under contract No. DE-AC52-07NA27344. B.A.B. acknowledges support from NSF Grant No. PHY-1811855.

[1] O. Sorlin and M.-G. Porquet, Prog. Part. Nucl. Phys. **61**, 602 (2008).
[2] T. Otsuka, A. Gade, O. Sorlin, T. Suzuki, and Y. Utsuno, Rev. Mod. Phys. **92**, 015002 (2020).
[3] A. Gade and S. N. Liddick, J. Phys. G **43**, 024001 (2016).
[4] E. Caurier, F. Nowacki, and A. Poves, Phys. Rev. C **90**, 014302 (2014).
[5] B. Bastin, S. Grévy, D. Sohler, O. Sorlin, Z. Dombrádi, N. L. Achouri, J. C. Angélique, F. Azaiez, D. Baiborodin, R. Borcea, C. Bourgeois, A. Buta, A. Bürger, R. Chapman, J. C. Dalouzy, Z. Dlouhy, A. Drouard, Z. Elekes, S. Franchoo, S. Iacob, B. Laurent, M. Lazar, X. Liang, E. Liénard, J. Mrazek, L. Nalpas, F. Negoita, N. A. Orr, Y. Penionzhkevich, Z. Podolyák, F. Pougheon, P. Roussel-Chomaz, M. G. Saint-Laurent, M. Stanoiu, I. Stefan, F. Nowacki, and A. Poves, Phys. Rev. Lett. **99**, 022503 (2007).
[6] S. Takeuchi, M. Matsushita, N. Aoi, P. Doornenbal, K. Li, T. Motobayashi, H. Scheit, D. Steppenbeck, H. Wang, H. Baba, D. Bazin, L. Càceres, H. Crawford, P. Fallon, R. Gernhäuser, J. Gibelin, S. Go, S. Grévy, C. Hinke, C. R. Hoffman, R. Hughes, E. Ideguchi, D. Jenkins, N. Kobayashi, Y. Kondo, R. Krücken, T. Le Bleis, J. Lee, G. Lee, A. Matta, S. Michimasa, T. Nakamura, S. Ota, M. Petri, T. Sako, H. Sakurai, S. Shimoura, K. Steiger, K. Takahashi, M. Takechi, Y. Togano, R. Winkler, and K. Yoneda, Phys. Rev. Lett. **109**, 182501 (2012).
[7] T. Glasmacher, B. A. Brown, M. J. Chromik, P. D. Cottle, M. Fauerbach, R. W. Ibbotson, K. W. Kemper, D. J. Morrissey, H. Scheit, D. W. Sklenicka, and M. Steiner, Phys. Lett. B **395**, 163 (1997).
[8] H. Scheit, T. Glasmacher, B. A. Brown, J. A. Brown, P. D. Cottle, P. G. Hansen, R. Harkewicz, M. Hellström, R. W. Ibbotson, J. K. Jewell, K. W. Kemper, D. J. Morrissey, M. Steiner, P. Thirolf, and M. Thoennessen, Phys. Rev. Lett. **77**, 3967 (1996).
[9] S. Grévy, F. Negoita, I. Stefan, N. L. Achouri, J. C. Angélique, B. Bastin, R. Borcea, A. Buta, J. M. Daugas, F. De Oliveira, O. Giarmana, C. Jollet, B. Laurent, M. Lazar, E. Liénard, F. Maréchal, J. Mrázek, D. Pantelica, Y. Penionzhkevich, S. Piétri, O. Sorlin, M. Stanoiu, C. Stodel, and M. G. St-Laurent, Eur. Phys. J. A **25**, 111 (2005).
[10] C. Force, S. Grévy, L. Gaudefroy, O. Sorlin, L. Cáceres, F. Rotaru, J. Mrazek, N. L. Achouri, J. C. Angélique, F. Azaiez, B. Bastin, R. Borcea, A. Buta, J. M. Daugas, Z. Dlouhy, Z. Dombrádi, F. De Oliveira, F. Negoita, Y. Penionzhkevich, M. G. Saint-Laurent, D. Sohler, M. Stanoiu, I. Stefan, C. Stodel, and F. Nowacki, Phys. Rev. Lett. **105**, 102501 (2010).
[11] D. Santiago-Gonzalez, I. Wiedenhöver, V. Abramkina, M. L. Avila, T. Baugher, D. Bazin, B. A. Brown, P. D. Cottle, A. Gade, T. Glasmacher, K. W. Kemper, S. McDaniel, A. Rojas, A. Ratkiewicz, R. Meharchand, E. C. Simpson, J. A. Tostevin, A. Volya, and D. Weisshaar, Phys. Rev. C **83**, 061305(R) (2011).
[12] J. J. Parker, I. Wiedenhöver, P. D. Cottle, J. Baker, D. McPherson, M. A. Riley, D. Santiago-Gonzalez, A. Volya, V. M. Bader, T. Baugher, D. Bazin, A. Gade, T. Ginter, H. Iwasaki, C. Loelius, C. Morse, F. Recchia, D. Smalley, S. R. Stroberg, K. Whitmore, D. Weisshaar, A. Lemasson, H. L. Crawford, A. O. Macchiavelli, and K. Wimmer, Phys. Rev. Lett. **118**, 052501 (2017).
[13] Y. Utsuno, N. Shimizu, T. Otsuka, T. Yoshida, and Y. Tsunoda, Phys. Rev. Lett. **114**, 032501 (2015).
[14] J. L. Egido, M. Borrajo, and T. R. Rodríguez, Phys. Rev. Lett. **116**, 052502 (2016).
[15] E. Lunderberg, A. Gade, V. Bader, T. Baugher, D. Bazin, J. S. Berryman, B. A. Brown, D. J. Hartley, F. Recchia, S. R. Stroberg, D. Weisshaar, and K. Wimmer, Phys. Rev. C **94**, 064327 (2016).
[16] Y. Utsuno, T. Otsuka, B. A. Brown, M. Honma, T. Mizusaki, and N. Shimizu, Phys. Rev. C **86**, 051301(R) (2012).
[17] B. Fornal, R. H. Mayer, I. G. Bearden, P. Benet, R. Broda, P. J. Daly, Z. W. Grabowski, I. Ahmad, M. P. Carpenter, P. B. Fernandez, R. V. F. Janssens, T. L. Khoo, T. Lauritsen, E. F. Moore, and M. Drigert, Phys. Rev. C **49**, 2413 (1994).
[18] A. Winther and K. Alder, Nucl. Phys. A **319**, 518 (1979).
[19] T. Glasmacher, Ann. Rev. Nucl. Part. Sci. **48**, 1 (1998).
[20] A. Gade, B. A. Brown, J. A. Tostevin, D. Bazin, P. C. Bender, C. M. Campbell, H. L. Crawford, B. Elman, K. W. Kemper, B. Longfellow, E. Lunderberg, D. Rhodes, and D. Weisshaar, Phys. Rev. Lett. **122**, 222501 (2019).
[21] L. A. Riley, D. Bazin, J. Belarge, P. C. Bender, B. A. Brown, P. D. Cottle, B. Elman, A. Gade, S. D. Gregory, E. B. Haldeman, K. W. Kemper, B. R. Klybor, M. A. Liggett, S. Lipschutz, B. Longfellow, E. Lunderberg, T. Mijatovic, J. Pereira, L. M. Skiles, R. Titus, A. Volya, D. Weisshaar, J. C. Zamora, and R. G. T. Zegers, Phys. Rev. C **100**, 044312 (2019).
[22] F. Nowacki and A. Poves, Phys. Rev. C **79**, 014310 (2009).
[23] B. Longfellow, D. Weisshaar, A. Gade, B. A. Brown, D. Bazin, K. W. Brown, B. Elman, J. Pereira, D. Rhodes, and M. Spieker, Phys. Rev. Lett. **125**, 232501 (2020).
[24] R. W. Ibbotson, T. Glasmacher, P. F. Mantica, and H. Scheit, Phys. Rev. C **59**, 642 (1999).
[25] A. Gade, D. Bazin, C. M. Campbell, J. A. Church, D. C. Dinca, J. Enders, T. Glasmacher, Z. Hu, K. W. Kemper, W. F. Mueller, H. Olliver, B. C. Perry, L. A. Riley, B. T. Roeder, B. M. Sherrill, and J. R. Terry, Phys. Rev. C **68**, 014302 (2003).
[26] S. Calinescu, L. Cáceres, S. Grévy, O. Sorlin, Z. Dombrádi, M. Stanoiu, R. Astabatyan, C. Borcea, R. Borcea, M. Bowry, W. Catford, E. Clément, S. Franchoo, R. Garcia, R. Gillibert, I. H. Guerin, I. Kuti, S. Lukyanov, A. Lepailleur, V. Maslov, P. Morfouace, J. Mrazek, F. Negoita, M. Niikura, L. Perrot, Z. Podolyák, C. Petrone, Y. Penionzhkevich, T. Roger, F. Rotaru, D. Sohler, I. Stefan, J. C. Thomas, Z. Vajta, and E. Wilson, Phys. Rev. C **93**, 044333 (2016).
[27] R. Winkler, A. Gade, T. Baugher, D. Bazin, B. A. Brown, T. Glasmacher, G. F. Grinyer, R. Meharchand, S. McDaniel, A. Ratkiewicz, and D. Weisshaar, Phys. Rev. Lett. **108**, 182501 (2012).
[28] A. Gade and B. M. Sherrill, Phys. Scr. **91**, 053003 (2016).
[29] D. Morrissey, B. Sherrill, M. Steiner, A. Stolz, and I. Wiedenhoever, Nucl. Instrum. Methods Phys. Res. B

204, 90 (2003).
[30] D. Bazin, J. Caggiano, B. Sherrill, J. Yurkon, and A. Zeller, Nucl. Instrum. Methods Phys. Res. B **204**, 629 (2003).
[31] J. Yurkon, D. Bazin, W. Benenson, D. Morrissey, B. Sherrill, D. Swan, and R. Swanson, Nucl. Instrum. Methods Phys. Res. A **422**, 291 (1999).
[32] A. Gade and T. Glasmacher, Prog. Part. Nucl. Phys. **60**, 161 (2008).
[33] J. M. Cook, T. Glasmacher, and A. Gade, Phys. Rev. C **73**, 024315 (2006).
[34] F. Delaunay and F. M. Nunes, J. Phys. G: Nucl. Part. Phys. **34**, 2207 (2007).
[35] D. Weisshaar, A. Gade, T. Glasmacher, G. F. Grinyer, D. Bazin, P. Adrich, T. Baugher, J. M. Cook, C. A. Diget, S. McDaniel, A. Ratkiewicz, K. P. Siwek, and K. A. Walsh, Nucl. Instrum. Methods Phys. Res. A **624**, 615 (2010).
[36] B. Elman, A. Gade, D. Weisshaar, D. Barofsky, D. Bazin, P. C. Bender, M. Bowry, M. Hjorth-Jensen, K. W. Kemper, S. Lipschutz, E. Lunderberg, N. Sachmpazidi, N. Terpstra, W. B. Walters, A. Westerberg, S. J. Williams, and K. Wimmer, Phys. Rev. C **96**, 044332 (2017).
[37] B. Longfellow, Ph.D. thesis, Michigan State University (2020).
[38] V. M. Bader, A. Gade, D. Weisshaar, B. A. Brown, T. Baugher, D. Bazin, J. S. Berryman, A. Ekström, M. Hjorth-Jensen, S. R. Stroberg, W. B. Walters, K. Wimmer, and R. Winkler, Phys. Rev. C **88**, 051301(R) (2013).
[39] B. Longfellow, A. Gade, B. A. Brown, W. A. Richter, D. Bazin, P. C. Bender, M. Bowry, B. Elman, E. Lunderberg, D. Weisshaar, and S. J. Williams, Phys. Rev. C **97**, 054307 (2018).
[40] Evaluated nuclear structure data file (ensdf), https://www.nndc.bnl.gov/ensdf/.
[41] J. W. Olness, E. K. Warburton, J. A. Becker, D. J. Decman, E. A. Henry, L. G. Mann, and L. Ussery, Phys. Rev. C **34**, 2049 (1986).
[42] E. K. Warburton, D. E. Alburger, and G. Wang, Phys. Rev. C **36**, 429 (1987).
[43] Z. M. Wang, R. Chapman, X. Liang, F. Haas, F. Azaiez, B. R. Behera, M. Burns, E. Caurier, L. Corradi, D. Curien, A. N. Deacon, Z. Dombrádi, E. Farnea, E. Fioretto, A. Gadea, A. Hodsdon, F. Ibrahim, A. Jungclaus, K. Keyes, V. Kumar, A. Latina, S. Lunardi, N. Mărginean, G. Montagnoli, D. R. Napoli, F. Nowacki, J. Ollier, D. O'Donnell, A. Papenberg, G. Pollarolo, M.-D. Salsac, F. Scarlassara, J. F. Smith, K. M. Spohr, M. Stanoiu, A. M. Stefanini, S. Szilner, M. Trotta, and D. Verney, Phys. Rev. C **81**, 054305 (2010).
[44] D. Sohler, Z. Dombrádi, J. Timár, O. Sorlin, F. Azaiez, F. Amorini, M. Belleguic, C. Bourgeois, C. Donzaud, J. Duprat, D. Guillemaud-Mueller, F. Ibrahim, J. A. Scarpaci, M. Stanoiu, M. J. Lopez, M. G. Saint-Laurent, F. Becker, F. Sarazin, C. Stodel, G. Voltolini, S. M. Lukyanov, V. Maslov, Y.-E. Penionzhkevich, M. Girod, S. Péru, F. Nowacki, G. Sletten, R. Lucas, C. Theisen, D. Baiborodin, Z. Dlouhy, J. Mrazek, C. Borcea, A. Bauchet, C. J. Moore, and M. J. Taylor, Phys. Rev. C **66**, 054302 (2002).
[45] K. L. Miller, Ph.D. thesis, Michigan State University (2003).
[46] K. L. Yurkewicz, D. Bazin, B. A. Brown, C. M. Campbell, J. A. Church, D. C. Dinca, A. Gade, T. Glasmacher, M. Honma, T. Mizusaki, W. F. Mueller, H. Olliver, T. Otsuka, L. A. Riley, and J. R. Terry, Phys. Rev. C **70**, 054319 (2004).
[47] T. Mijatović, N. Kobayashi, H. Iwasaki, D. Bazin, J. Belarge, P. C. Bender, B. A. Brown, A. Dewald, R. Elder, B. Elman, A. Gade, M. Grinder, T. Haylett, S. Heil, C. Loelius, B. Longfellow, E. Lunderberg, M. Mathy, K. Whitmore, and D. Weisshaar, Phys. Rev. Lett. **121**, 012501 (2018).
[48] L. Cáceres, D. Sohler, S. Grévy, O. Sorlin, Z. Dombrádi, B. Bastin, N. L. Achouri, J. C. Angélique, F. Azaiez, D. Baiborodin, R. Borcea, C. Bourgeois, A. Buta, A. Bürger, R. Chapman, J. C. Dalouzy, Z. Dlouhy, A. Drouard, Z. Elekes, S. Franchoo, L. Gaudefroy, S. Iacob, B. Laurent, M. Lazar, X. Liang, E. Liénard, J. Mrazek, L. Nalpas, F. Negoita, F. Nowacki, N. A. Orr, Y. Penionzhkevich, Z. Podolyák, F. Pougheon, A. Poves, P. Roussel-Chomaz, M. G. Saint-Laurent, M. Stanoiu, and I. Stefan, Phys. Rev. C **85**, 024311 (2012).
[49] L. A. Riley, P. Adrich, N. Ahsan, T. R. Baugher, D. Bazin, B. A. Brown, J. M. Cook, P. D. Cottle, C. A. Diget, A. Gade, T. Glasmacher, K. E. Hosier, K. W. Kemper, A. Ratkiewicz, K. P. Siwek, J. A. Tostevin, A. Volya, and D. Weisshaar, Phys. Rev. C **86**, 047301 (2012).
[50] S. R. Stroberg, A. Gade, J. A. Tostevin, V. M. Bader, T. Baugher, D. Bazin, J. S. Berryman, B. A. Brown, C. M. Campbell, K. W. Kemper, C. Langer, E. Lunderberg, A. Lemasson, S. Noji, F. Recchia, C. Walz, D. Weisshaar, and S. J. Williams, Phys. Rev. C **90**, 034301 (2014).
[51] K. Nowak, K. Wimmer, S. Hellgartner, D. Mücher, V. Bildstein, J. Diriken, J. Elseviers, L. P. Gaffney, R. Gernhäuser, J. Iwanicki, J. G. Johansen, M. Huyse, J. Konki, T. Kröll, R. Krücken, R. Lutter, R. Orlandi, J. Pakarinen, R. Raabe, P. Reiter, T. Roger, G. Schrieder, M. Seidlitz, O. Sorlin, P. Van Duppen, N. Warr, H. De Witte, and M. Zielińska, Phys. Rev. C **93**, 044335 (2016).
[52] S. Momiyama, K. Wimmer, D. Bazin, J. Belarge, P. Bender, B. Elman, A. Gade, K. W. Kemper, N. Kitamura, B. Longfellow, E. Lunderberg, M. Niikura, S. Ota, P. Schrock, J. A. Tostevin, and D. Weisshaar, Phys. Rev. C **102**, 034325 (2020).
[53] A. Gade, B. A. Brown, D. Bazin, C. M. Campbell, J. A. Church, D. C. Dinca, J. Enders, T. Glasmacher, M. Horoi, Z. Hu, K. W. Kemper, W. F. Mueller, T. Otsuka, L. A. Riley, B. T. Roeder, T. Suzuki, J. R. Terry, K. L. Yurkewicz, and H. Zwahlen, Phys. Rev. C **74**, 034322 (2006).
[54] S. R. Stroberg, A. Gade, T. Baugher, D. Bazin, B. A. Brown, J. M. Cook, T. Glasmacher, G. F. Grinyer, S. McDaniel, A. Ratkiewicz, and D. Weisshaar, Phys. Rev. C **86**, 024321 (2012).
[55] D. Mengoni, J. J. Valiente-Dobón, A. Gadea, S. Lunardi, S. M. Lenzi, R. Broda, A. Dewald, T. Pissulla, L. J. Angus, S. Aydin, D. Bazzacco, G. Benzoni, P. G. Bizzeti, A. M. Bizzeti-Sona, P. Boutachkov, L. Corradi, F. Crespi, G. de Angelis, E. Farnea, E. Fioretto, A. Goergen, M. Gorska, A. Gottardo, E. Grodner, A. M. Howard, W. Królas, S. Leoni, P. Mason, D. Montanari, G. Montagnoli, D. R. Napoli, A. Obertelli, R. Orlandi,

T. Pawłat, G. Pollarolo, F. Recchia, A. Algora, B. Rubio, E. Sahin, F. Scarlassara, R. Silvestri, J. F. Smith, A. M. Stefanini, D. Steppenbeck, S. Szilner, C. A. Ur, P. T. Wady, and J. Wrzesiński, Phys. Rev. C **82**, 024308 (2010).

[56] K. Kaneko, Y. Sun, T. Mizusaki, and M. Hasegawa, Phys. Rev. C **83**, 014320 (2011).

[57] A. Gade, J. A. Tostevin, V. Bader, T. Baugher, D. Bazin, J. S. Berryman, B. A. Brown, C. A. Diget, T. Glasmacher, D. J. Hartley, E. Lunderberg, S. R. Stroberg, F. Recchia, A. Ratkiewicz, D. Weisshaar, and K. Wimmer, Phys. Rev. C **93**, 054315 (2016).

[58] W. A. Richter, S. Mkhize, and B. A. Brown, Phys. Rev. C **78**, 064302 (2008).

[59] M. Honma, T. Otsuka, B. A. Brown, and T. Mizusaki, Phys. Rev. C **69**, 034335 (2004).

[60] B. Pritychenko, M. Birch, B. Singh, and M. Horoi, At. Data Nucl. Data Tables **107**, 1 (2016).

[61] B. Brown, A. Arima, and J. McGrory, Nucl. Phys. A **277**, 77 (1977).

[62] S. Heil, M. Petri, K. Vobig, D. Bazin, J. Belarge, P. Bender, B. Brown, R. Elder, B. Elman, A. Gade, T. Haylett, J. Holt, T. Hüther, A. Hufnagel, H. Iwasaki, N. Kobayashi, C. Loelius, B. Longfellow, E. Lunderberg, M. Mathy, J. Menéndez, S. Paschalis, R. Roth, A. Schwenk, J. Simonis, I. Syndikus, D. Weisshaar, and K. Whitmore, Phys. Lett. B **809**, 135678 (2020).

[63] W. Gerace and A. Green, Nucl. Phys. A **93**, 110 (1967).

[64] E. Caurier, J. Menéndez, F. Nowacki, and A. Poves, Phys. Rev. C **75**, 054317 (2007).

[65] K. Hadyńska-Klęk, P. J. Napiorkowski, M. Zielińska, J. Srebrny, A. Maj, F. Azaiez, J. J. Valiente Dobón, M. Kicińska-Habior, F. Nowacki, H. Naïdja, B. Bounthong, T. R. Rodríguez, G. de Angelis, T. Abraham, G. Anil Kumar, D. Bazzacco, M. Bellato, D. Bortolato, P. Bednarczyk, G. Benzoni, L. Berti, B. Birkenbach, B. Bruyneel, S. Brambilla, F. Camera, J. Chavas, B. Cederwall, L. Charles, M. Ciemała, P. Cocconi, P. Coleman-Smith, A. Colombo, A. Corsi, F. C. L. Crespi, D. M. Cullen, A. Czermak, P. Désesquelles, D. T. Doherty, B. Dulny, J. Eberth, E. Farnea, B. Fornal, S. Franchoo, A. Gadea, A. Giaz, A. Gottardo, X. Grave, J. Grębosz, A. Görgen, M. Gulmini, T. Habermann, H. Hess, R. Isocrate, J. Iwanicki, G. Jaworski, D. S. Judson, A. Jungclaus, N. Karkour, M. Kmiecik, D. Karpiński, M. Kisieliński, N. Kondratyev, A. Korichi, M. Komorowska, M. Kowalczyk, W. Korten, M. Krzysiek, G. Lehaut, S. Leoni, J. Ljungvall, A. Lopez-Martens, S. Lunardi, G. Maron, K. Mazurek, R. Menegazzo, D. Mengoni, E. Merchán, W. Męczyński, C. Michelagnoli, B. Million, S. Myalski, D. R. Napoli, M. Niikura, A. Obertelli, S. F. Özmen, M. Palacz, L. Próchniak, A. Pullia, B. Quintana, G. Rampazzo, F. Recchia, N. Redon, P. Reiter, D. Rosso, K. Rusek, E. Sahin, M.-D. Salsac, P.-A. Söderström, I. Stefan, O. Stézowski, J. Styczeń, C. Theisen, N. Toniolo, C. A. Ur, R. Wadsworth, B. Wasilewska, A. Wiens, J. L. Wood, K. Wrzosek-Lipska, and M. Zięblíński, Phys. Rev. C **97**, 024326 (2018).

[66] B. A. Brown and W. A. Richter, Phys. Rev. C **58**, 2099 (1998).

[67] T. Miyagi, S. R. Stroberg, J. D. Holt, and N. Shimizu, Phys. Rev. C **102**, 034320 (2020).